Chair of Materials Physics

Master's Thesis

Analysis of the strain information from nanodiffraction data

Lukas Schretter, BSc

February 2021

I

EIDESSTATTLICHE ERKLÄRUNG

Ich erkläre an Eides statt, dass ich diese Arbeit selbständig verfasst, andere als die angegebenen Quellen und Hilfsmittel nicht benutzt, und mich auch sonst keiner unerlaubten Hilfsmittel bedient habe.

Ich erkläre, dass ich die Richtlinien des Senats der Montanuniversität Leoben zu "Gute wissenschaftliche Praxis" gelesen, verstanden und befolgt habe.

Weiters erkläre ich, dass die elektronische und gedruckte Version der eingereichten wissenschaftlichen Abschlussarbeit formal und inhaltlich identisch sind.

Datum 15.02.2021

Unterschrift Verfasser/in
Lukas Schretter

Abstract

Nano beam electron diffraction is a powerful technique used for strain determination in thin crystalline and amorphous samples, as it combines high spatial resolution, accuracy, and precision. The influence of three-dimensional strain fields in samples, which are mostly present due to complex strain states or effects of free surface relaxations, is still unknown today. This study aims to increase the understanding of the averaging of the Bragg angle and the impact of such three-dimensional strain fields on the measured strain.

To analyze the effect of a three-dimensional strain field on the average diffraction angle and strain evaluation, a combination of finite element and diffraction simulations was carried out. Specimen were modeled and deformed using finite element analysis. The atom positions were then interpolated into the finite element mesh and an electron diffraction simulation was executed. The obtained diffraction images were then evaluated using the square-root magnitude weighted phase correlation method. The resulting strain values were compared to the actual strain in the samples obtained from the finite element models.

The simulations showed that the measured strains are in good agreement with the average strain along the microscope optical axis. However, a strong dependency of the measured strain from the angular deviation could be found. For higher absolute strain values and gradients, the diffraction simulations led to distorted images, but the strain evaluation using the square-root magnitude weighted phase correlation still yielded good results, proving the immense stability of this technique.

Kurzfassung

Nano-Elektronenbeugung vereint die Aspekte hoher räumlicher Auflösung, hoher Genauigkeit und hoher Präzision, wodurch sie zu einer der leistungsstärksten Methoden zur Dehnungsbestimmung in dünnen kristallinen und amorphen Proben zählt. Der genaue Einfluss dreidimensionaler Dehnungsfelder in den Proben, die meist bedingt durch komplexe Dehnungszustände oder durch Effekte der Oberflächenrelaxationen vorherrschen, ist bis heute ungeklärt. Das Ziel dieser Studie ist die Analyse der Mittelung des Bragg-Winkels, um den Einfluss solcher Dehnungsfelder auf die gemessene Dehnung genauer bestimmen zu können.

Um diese Analyse durchzuführen, wurde eine Kombination aus Finite-Elemente-Simulationen und Beugungssimulationen gewählt. Die Proben wurden unter Verwendung der Finite-Elemente-Methode modelliert und verformt. Anschließend wurden die Atompositionen in das Finite-Elemente-Netz interpoliert und eine Elektronenbeugungssimulation durchgeführt. Die erhaltenen Beugungsbilder wurden unter Verwendung der square-root-magnitude-weighted-phase-correlation-Methode ausgewertet. Die resultierenden Dehnungen wurden mit den tatsächlichen Dehnungen der Proben verglichen, die den Finite-Elemente-Modellen entnommen wurden.

Die Simulationen zeigten, dass die gemessenen Dehnungen sehr gut mit der mittleren Dehnung entlang der optischen Achse des Transmissions-elektronenmikroskops übereinstimmen. Es konnte eine starke Abhängigkeit der gemessenen Dehnung von der Winkelabweichung zwischen der Zonenachse und der optischen Achse festgestellt werden. Beim Vorliegen höherer absoluter Dehnungen sowie Dehnungsgradienten führte die Beugungssimulation zu stark verzerrten Bildern. Die Auswertung dieser verzerrten Beugungsbilder unter Verwendung der square-root-magnitude-weighted-phase-correlation-Methode ergab trotzdem gute Ergebnisse für die gemessenen Dehnungen. Das zeigt die große Stabilität dieser Technik.

Table of contents

1 Introduction

Accurate determination of strains with high spatial resolution is one of the keys for a greater understanding of many physical phenomena and towards improving material properties. For example, the deformation behavior of metals is fundamentally controlled by nanoscale strain fields surrounding defects in the material. Furthermore, a huge focus of the semiconductor industry is strain engineering, as the application of strain can be used to enhance charge carrier mobility [1]. Presently, transmission electron microscopy (TEM) is the only tool allowing for strain determination with spatial resolutions in the low nanometer range. A variety of techniques have been developed, such as converged and nano beam electron diffraction, dark field electron holography or high resolution TEM, each possessing its own advantages and drawbacks [2,3].

Nano beam electron diffraction (NBED) uses a near parallel, nanometer sized electron probe which scans across the specimen. At each point, independent diffraction images are recorded with high resolution, which are then used for the strain determination. Modern TEMs achieve probe sizes below 1 nm, resulting in excellent spatial resolution. As the probe scans across the specimen, the field of view can be made extremely large. The determination of strain from diffraction images is pretty straight forward, and advances in peak finding algorithms allow for sub pixel resolution. More recent developments include the use of patterned electron probes [4] and precession NBED [5], which further improve the strain precision up to $2 \cdot 10^{-4}$. Despite all these advances, the effect of a three-dimensional strain field on the measurement has not been studied to date. If a strain gradient along the electron beam direction is present, the lattice constant changes with increasing penetration depth, thus resulting in a local variation of the Bragg angle. The total diffraction angle, respectively the derived strain, should therefore be some sort of an average along the microscope optical axis.

This thesis aims to investigate the effect of averaging the Bragg angle in NBED experiments on specimens with a three-dimensional strain field. To properly examine this effect, it is essential to know the exact strain field in the sample. Hence, a simulation study was chosen to be best suited, especially since modern TEM image simulations provide results of high accuracy. Deformed specimens were modelled using finite element analysis (FEA), and subsequently STEM simulations were carried out on the distorted lattice. From the obtained diffraction images, the strain was evaluated and compared to the known results of the FEA to determine the effect of the three-dimensional strain field on the acquired data.

[1]

2 Dynamical theory of electron diffraction

In the classical kinematical theory of diffraction only single scattering is assumed. In the case of electron diffraction, this description is, however, only sufficient if the specimen is extremely thin. For thicker samples, multiple scattering must be considered, which the kinematical theory does not account for. As a result, a new method was developed, widely known as the dynamical theory. This is based on solving the Schrödinger equation for the imaging electrons inside the specimen [6–8]. In the following sections, the physical principles of these calculations will be described. The theoretical treatment will further be restricted to the imaging conditions in a TEM. First, the wave equation for fast electrons will be derived. Second, the most common methods used to solve the problem are presented.

The mathematical descriptions in the following sections will primarily be taken from Kirkland [9] as his book provides an excellent overview of the concepts in dynamical electron diffraction. Furthermore, this ensures a consistent description.

2.1 Theory of high energy electron diffraction

As already mentioned, the problem of the elastic scattering of fast electrons by an atom is described by the Schrödinger equation. Under the typical conditions present in a TEM, the imaging electrons travel at a significant fraction of the speed of light. Hence, the Schrödinger equation is no longer appropriate, and the relativistic Dirac equation should be used. However, the effects of electron spin are negligible, and the use of the Dirac equation makes calculations far more complicated. The relativistic effects can also be adequately treated by using the Schrödinger equation with relativistically corrected mass and wavelength [10]. Further, the image is assumed to be stationary, thus time dependency is neglected [9].

$$\left[-\frac{\hbar^2}{2m} \nabla^2 - eV(x,y,z) \right] \Psi(x,y,z) = E\Psi(x,y,z) \tag{1}$$

Here Ψ is the electron wave function, $\hbar = h/2\pi$ is Planck's constant divided by 2π, ∇^2 is the Nabla operator squared (respectively the Laplacian), e is the elementary charge, V is the electrostatic potential in the specimen and E is the kinetic energy of the imaging electrons. The relativistic corrected mass m and wavelength λ are defined by:

$$m = m_0 + \frac{eV}{c^2} \tag{2}$$

[2]

$$\lambda = \frac{hc}{\sqrt{eV(2m_0c^2 + eV)}} \tag{3}$$

where c is the speed of light and m_0 is the electron rest mass. Only elastic scattering will be assumed, so the kinetic energy stays constant and is given by:

$$E = \frac{h^2}{2m\lambda^2} \tag{4}$$

As the imaging electrons penetrate the specimen, they gain potential energy due to the electrostatic attraction to the positively charged nuclei. Since the electrons in the TEM possess very high kinetic energies, this change in potential energy is very weak and the electrons motions are only slightly perturbated. It is therefore useful to separate the large velocity in z-direction from the effects due to the interaction with the specimen. Thus, the complete electron wave function Ψ is separated into a plane wave traveling along the z-axis and a factor $\psi(x, y, z)$ that slowly varies with depth z and represents the perturbations due to the interactions with the specimen [11]:

$$\Psi(x, y, z) = \psi(x, y, z) \cdot exp(2\pi i z/\lambda) \tag{5}$$

To use Equation (5) in (1) requires calculating $\nabla^2\psi$. To do this, first the ∇^2 is split into a z-directional and a transversal part.

$$\nabla^2 = \left[\frac{\partial^2}{\partial x^2} + \frac{\partial^2}{\partial y^2} + \frac{\partial^2}{\partial z^2}\right] = \left[\nabla^2_{xy} + \frac{\partial^2}{\partial z^2}\right] \tag{6}$$

Combining Equations (5) and (6) the derivatives of Ψ with respect to x and y are calculated.

$$\nabla^2\Psi = \left[\nabla^2_{xy} + \frac{\partial^2}{\partial z^2}\right]\Psi = exp(2\pi i z/\lambda)\nabla^2_{xy}\psi + \frac{\partial^2}{\partial z^2}[\psi \, exp(2\pi i z/\lambda)] \tag{7}$$

Next, the derivatives with respect to z need to be solved.

$$\frac{\partial}{\partial z}[\psi \exp(2\pi i z / \lambda)] = \exp(2\pi i z/\lambda)\left[\frac{\partial\psi}{\partial z} + \frac{2\pi i}{\lambda}\psi\right] \tag{8}$$

$$\frac{\partial^2}{\partial z^2}[\psi \exp(2\pi i z / \lambda)] = \exp(2\pi i z/\lambda)\left[\frac{\partial^2\psi}{\partial z^2} + \frac{4\pi i}{\lambda}\frac{\partial\psi}{\partial z}\right] - \frac{4\pi^2}{\lambda^2}\psi \tag{9}$$

Equation (9) can now be inserted into (1). With (4) the term on the far right in (9) cancels out and dropping the factor $exp(2\pi i z/\lambda)$ leads to:

$$-\frac{\hbar^2}{2m}\left[\nabla_{xy}^2 + \frac{\partial^2}{\partial z^2} + \frac{4\pi i}{\lambda}\frac{\partial}{\partial z} + \frac{2meV(x,y,z)}{\hbar^2}\right]\psi(x,y,z) = 0 \qquad (10)$$

Equation (10) is mathematically identical to (1) as no approximations were made up to this point. Now however, the paraxial approximation is introduced. The second order derivative in Equation (10) is dropped as it is assumed that ψ varies slowly with depth z inside the specimen, which is often referred to as neglecting backscattering [11]. Also dropping the pre-factor on the left-hand side of Equation (10), it can be written as a first order differential equation [8,9].

$$\begin{aligned}\frac{\partial\psi(x,y,z)}{\partial z} &= \left[\frac{i\lambda}{4\pi}\nabla_{xy}^2 + \frac{2mei\lambda}{4\pi\hbar^2}V(x,y,z)\right]\psi(x,y,z) = \\ &= \left[\frac{i\lambda}{4\pi}\nabla_{xy}^2 + i\sigma V(x,y,z)\right]\psi(x,y,z)\end{aligned} \qquad (11)$$

where $\sigma = 2\pi me\lambda / h^2$ is the interaction parameter. Finally, Equation (11) describes the elastic interactions between the specimen and the imaging electrons. However, this equation has still no obvious solution and is rather hard to solve. In principle, there are two different methods today which try to solve the problem: the Bethe-Bloch-Wave method and the Multislice method. While the Bethe-Bloch-Wave method solves Equation (11) analytically, the Multislice method tries to solve it numerically. In addition, there are also some hybrid methods using aspects of both theories, such as the PRISM algorithm used in this study.

2.2 Bethe-Bloch-Wave method

The Bloch wave method was first introduced by Bethe [12] in 1928 and is based on direct solution of Equation (11) using Bloch's theorem. This theorem states that in a periodic potential, the solutions to the Schrödinger equation take the form of a plane wave modulated by a function with the same periodicity as the potential [13]. This means, that the solution to Equation (11) can be built from a plane wave and a function with the periodicity of the crystal. This implicitly states however that the specimen must represent a crystal with perfect periodicity [9,14].

As the Bloch wave method allows for an analytical solution, it can provide fundamental physical insights which cannot be achieved by numerical methods [15].

Here, the well-known Howie-Whelan equations [16] will be derived. As the crystal potential needs to be perfectly periodic, it can be expanded into a Fourier series:

$$V(x, y, z) = V(\boldsymbol{r}) = \sum_{G} V_{\boldsymbol{G}} \exp[2\pi i \boldsymbol{G} \cdot \boldsymbol{r}] \tag{12}$$

where $\boldsymbol{G} = (G_x + G_y + G_z)$ is a set of reciprocal lattice vectors of the specimen and $V_{\boldsymbol{G}}$ is the potential at the reciprocal lattice site $\boldsymbol{G}$ (the bold letters indicate vectors). Using this Fourier series and Bloch's theorem, the slowly varying part of the electron wave function ψ can easily be described by a Bloch wave function in the form of Equation 13 [9,16,17].

$$\psi(x, y, z) = \psi(\boldsymbol{r}) = \sum_{G} \phi_{\boldsymbol{G}}(z) \exp[2\pi i \boldsymbol{G} \cdot \boldsymbol{r}] \tag{13}$$

The Fourier coefficients $\phi_{\boldsymbol{G}}$ are slowly varying with depth z in the specimen. Substituting Equations (12) and (13) into (11) and dropping the common factor $\exp[2\pi i \boldsymbol{G} \cdot \boldsymbol{r}]$ yields:

$$\frac{\partial \phi_{\boldsymbol{G}}(z)}{\partial z} = -\pi i \big(2G_z + \lambda G_x^2 + \lambda G_y^2\big)\phi_{\boldsymbol{G}}(z) + i\sigma \sum_{G'} V_{\boldsymbol{G}-\boldsymbol{G}'}\phi_{\boldsymbol{G}'}(z) =$$
$$= 2\pi i s_{\boldsymbol{G}}\phi_{\boldsymbol{G}}(z) + i\sigma \sum_{G'} V_{\boldsymbol{G}-\boldsymbol{G}'}\phi_{\boldsymbol{G}'}(z) \tag{14}$$

where the excitation error $s_{\boldsymbol{G}} = G_z + {}^{1}\!/_{2}\,\lambda\big(G_x^2 + G_y^2\big)$ is introduced and describes the deviation from the Bragg condition [6]. The derived set of first order differential equations is widely known as the Howie-Whelan equations. This set of equations can be solved using standard computer aided differential equation techniques.

As all coefficients $\phi_{\boldsymbol{G}}$ are known, the wavefunction in the specimen must be matched to the incident electron function via weighting coefficients $\alpha_{\boldsymbol{G}}$.

$$\psi_{incident}(z = 0) = \sum_{G} \alpha_{\boldsymbol{G}}\, \phi_{\boldsymbol{G}}(z = 0) \exp[2\pi i \boldsymbol{G} \cdot \boldsymbol{r}] \tag{15}$$

Sturkey [18] shows how this problem can be restated into a scattering matrix approach. The scattering matrix $\boldsymbol{S}$ connects the outgoing and incoming wave functions in the form of:

$$\psi_{exit} = \boldsymbol{S}\,\psi_{incident} \tag{16}$$

In principle, the Bloch wave method can be solved by hand for small unit cells requiring only two or three beams, respectively Fourier coefficients. For larger unit cell sizes the number of necessary beams increases drastically making even computer aided calculations very inefficient [9].

2.3 Multislice Method

In this section the Multislice method will be described. First the physical principles of transmission and beam propagation are explained. Second, the Multislice equation will be derived from the Schrödinger equation as given by Equation (11).
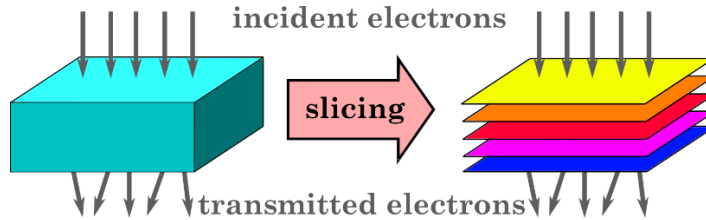
2.3.1 Physical background

Figure 1: *Illustration of the slicing of the specimen along the beam axis.*

The Multislice method is based on the physical optics theory developed by Cowley and Moodie [19]. In this method, the specimen is divided into thin slices normal to the incident beam direction as shown in Figure 1. Each of these slices must be thin enough to be treated as a weak phase object. In a weak phase object, the imaging electrons pass through with only a small deviation to their paths. This change in path can equivalently be treated as a change in wavelength or phase [9,20]. It is further assumed that the effect of the 3D specimen potential can be replaced by a 2D object, the so called projected potential v_z. Hence, the potential is integrated over the slice thickness along the z-axis [6,21].

$$v_z(x,y) = \int V(x,y,z)dz \tag{17}$$

Knowing the incident electron wave function ψ_{in}, the outgoing scattered wavefunction ψ_{out} can be calculated as:

$$\psi_{out}(x,y) = \exp[i\sigma v_z(x,y)] \exp(2\pi i k_z z) = t(x,y)\,\psi_{in}(x,y) \tag{18}$$

where $t(x,y)$ is the transmission function through one slice. The single slices are, however, separated by a distance Δz and a description for the wave propagation between the slices is needed. This propagation is based on Huygens principle, which states that every point of a wave front gives rise to an outgoing spherical wave. These spherical waves propagate to the next slice, interfere with each other, and build up the next ingoing wave. An illustration of that principle is shown in Figure 2. This phenomenon can be described using the Fresnel-Kirchhoff diffraction integral (Equation 19) [9,22].

[6]

$$\psi(x, y, z + \Delta z) = \frac{1}{i\lambda} \int \psi(x', y', z) \frac{\exp(2\pi i R / \lambda)}{R} (1 + \cos\theta) \, dx' \, dy' \tag{19}$$

where R is the propagation distance from the point (x', y', z) to point $(x, y, z + \Delta z)$ as shown in Figure 2. For fast electrons, the scattering angle is very small so $\cos\theta$ is approximately one and the distance R might be approximated as [6,9]:

$$R = \sqrt{(x - x')^2 + (y - y')^2 + \Delta z^2} \approx \Delta z \left(1 + \frac{1}{2} \frac{(x - x')^2}{\Delta z} + \frac{1}{2} \frac{(y - y')^2}{\Delta z}\right) \tag{20}$$
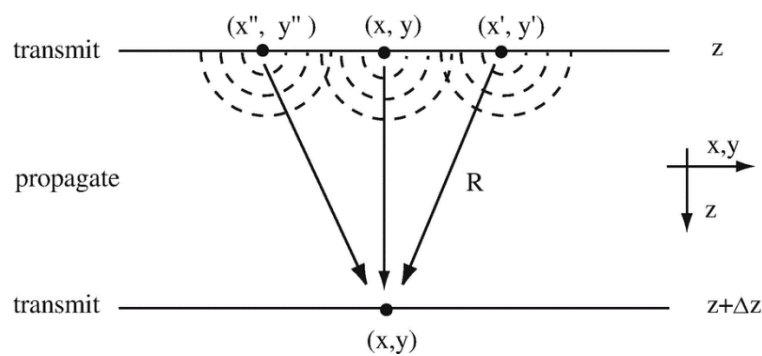
Figure 2: *Illustration of Huygens principle for the propagation between the slices at z and z + Δz. Each point of the wavefront at z gives rise to an outgoing spherical wave [9].*

This leads to the simplified diffraction integral in the form of Equation (21).

$$\psi(x, y, z + \Delta z) =$$
$$= \frac{1}{2i\lambda} \frac{\exp(2\pi i \Delta z / \lambda)}{\Delta z} \int \psi(x', y', z) \, \exp\left\{\frac{i\pi}{\lambda \Delta z} [(x - x')^2 + (y - y')^2]\right\} dx' \, dy' \tag{21}$$

Equation (21) can be rewritten in terms of a propagator function $p(x, y, \Delta z)$ and a convolution as follows:

$$\psi(x, y, z + \Delta z) = \exp(2\pi i \Delta z / \lambda) \left[\psi(x, y, z) \otimes p(x, y, \Delta z)\right] \tag{22}$$

$$p(x, y, \Delta z) = \frac{1}{i\lambda \Delta z} \exp\left[\frac{i\pi}{\lambda \Delta z}(x^2 + y^2)\right] \tag{23}$$

Using Equations (18) and (22), the Multislice equation for the propagation through one slice can be written as:

$$\psi(x, y, z + \Delta z) = p(x, y, \Delta z) \otimes [t(x, y) \, \psi(x, y, z)] \tag{24}$$

[7]

2.3.2 Deriving the Multislice equation

Next, the Multislice equation will be derived, starting from the Schrödinger equation to show that the physical principles from the section before can be used to describe the electron diffraction in the TEM. The Schrödinger equation (11) can be written in operator form as:

$$\frac{\partial \psi(x,y,z)}{\partial z} = [A + B]\psi(x,y,z) \tag{25}$$

with the non-commutative operators:

$$A = \frac{i\lambda}{4\pi} \nabla_{xy}^2 \tag{26}$$

$$B = i\sigma V(x,y,z) \tag{27}$$

The formal operator solution to Equation (24) is given by:

$$\psi(x,y,z) = \exp\left[\int_0^z [A(z') + B(z')]\, dz'\right] \psi(x,y,0) \tag{28}$$

The solution for one slice is obtained by integration of Equation 28 from z to $z + \Delta z$. Substituting the operators back into (28) yields:

$$\psi(x,y,z+\Delta z) = \exp\left[\int_z^{z+\Delta z} \left(\frac{i\lambda}{4\pi} \nabla_{xy}^2 + i\sigma V(x,y,z)\right) dz'\right] \psi(x,y,z) \tag{29}$$

For $\Delta z \to 0$, Equation (29) ca be approximated as:

$$\psi(x,y,z+\Delta z) = \exp\left[\frac{i\lambda}{4\pi} \Delta z \nabla_{xy}^2 + i\sigma v_{\Delta z}(x,y,z)\right] \psi(x,y,z) \tag{30}$$

where $v_{\Delta z}$ is the projected potential between z and $z + \Delta z$ (compare Equation (17)). The appearance of the operator ∇_{xy}^2 in the exponential of the right-hand side of Equation (30) complicates the solution, but with some mathematical manipulation (compare Kirkland [9] section 6.4), it can be rewritten as:

$$\psi(x,y,z+\Delta z) = \exp\left(\frac{i\lambda\Delta z}{4\pi} \nabla_{xy}^2\right) \exp[i\sigma v_{\Delta z}(x,y,z)] \psi(x,y,z) + \mathcal{O}(\Delta z^2) \tag{31}$$

The introduction of the approximations led to the error term $\mathcal{O}(\Delta z^2)$, where the magnitude of the error is of magnitude Δz^2. To be more precise, the error term should actually be written as $\mathcal{O}(\Delta z^2 v_{\Delta z})$ meaning that the Multislice equation is more accurate the smaller the projected potential. Therefore, the simulations

should be more accurate for light atoms [9]. Comparing this result to Equation (18), the transmission function can be defined according to [8,9] as follows:

$$t(x, y, z) = \exp[i\sigma v_{\Delta z}(x, y, z)] \tag{32}$$

The remaining exponential is more complicated to interpret. In principle, a Fourier transformation of Equation (31) is made. The operator ∇_{xy}^2 is then split into $\partial^2/\partial x^2 + \partial^2/\partial y^2$, and the resulting two exponentials are expanded into power series. Repeated integration and the assumption that $t\psi$ obeys periodic boundary condition yields:

$$FT\left[\exp\left(\frac{i\lambda\Delta z}{4\pi}\nabla_{xy}^2\right)(t\psi)\right] = \exp\left[-i\pi\lambda\Delta z\left(k_x^2 + k_y^2\right)\right]FT[(t\psi)] = P(k, \Delta z)FT[t\psi] \tag{33}$$

Where $k = \left(k_x^2 + k_y^2\right)^{1/2}$ and $P(k, \Delta z)$ is the propagator function in Fourier space. This propagator can also be written in real space with a convolution [8], leading to the same result as the previously shown Fresnel propagator (Equation (23)).

$$p(x, y, \Delta z) \otimes = \frac{1}{i\lambda\Delta z}\exp\left(\frac{i\pi}{\lambda\Delta z}(x^2 + y^2)\right) \otimes \tag{34}$$

Now the Multislice equation in real space can be written as:

$$\psi(x, y, z + \Delta z) = p(x, y, \Delta z) \otimes [t(x, y, z)\psi(x, y, z)] + \mathcal{O}(\Delta z^2) \tag{35}$$

This equation describes the wave transmission and propagation through one slice. For the calculation of the interaction with the whole sample, this function must be used multiple times to alternately transmit and propagate the wave function.

2.4 The PRISM-algorithm

The PRISM-algorithm developed by Ophus [23] tries to combine features of both methods explained above. The aim is to achieve a method for calculating images of thousands of STEM probe positions with a speed up compared to the traditional methods. Even though the Multislice method is already quite efficient for larger specimens compared to the Bloch wave method, it is still not practical for the calculation of thousands of STEM probe positions, as Equation (35) must be evaluated independently for each probe position. Ophus therefore reformulated the STEM simulations into a scattering-matrix approach, where the computational load of applying the Multislice Equation (35) to solve Equation (11) is shared between different probe positions. Furthermore, an interpolation factor is introduced, which reduces the number of plane waves used, leading to a further decrease in computational load.

First, the specimen is divided into slices and the projected potential for each slice is calculated as in the Multislice method. Second, the interpolation factor f is chosen. Typical values for f range from 4 to 20, but to choose the proper factor it is recommended to simply simulate a few probes.

The electron probe is determined as a set of plane waves given by:

$$\Psi_{m,n}(\boldsymbol{k}) = \delta(k_x - mf\Delta k, \; k_y - mf\Delta k) \tag{36}$$

where m and n are the indices of the plane waves, $\delta(\boldsymbol{k})$ is the delta function and Δk is the Fourier space pixel size. The plane waves are limited by:

$$\sqrt{m^2 + n^2}\, f\lambda\Delta k \leq \alpha_{max} \tag{37}$$

where α_{max} is the maximum probe angle to be considered. The Multislice simulation is then performed for each of these incident plane waves. From Equation (36), it can be seen that the number of plane waves calculated is reduced by a factor f^2. The plane waves are stored in real space in a scattering matrix $\boldsymbol{S}$. Then each converged electron probe at position $\boldsymbol{r}_0 = (x_0, y_0)$ is computed by first computing the required coefficients $\alpha_{m,n}(\boldsymbol{r}_0)$ for each plane wave $S_{m,n}(\boldsymbol{r})$ using:

$$\alpha_{m,n}(\boldsymbol{r}_0) = A(\boldsymbol{k}) \exp[-i\chi(\boldsymbol{k})] \; exp[2i\pi\boldsymbol{k} - (x_0 - h\tan(\theta_x), y_0 - h\tan(\theta_y))] \tag{38}$$

where $A(\boldsymbol{k})$ is the probe aperture function, $\chi(\boldsymbol{k})$ is the phase shift function which corrects for the aberrations in the TEM and the terms $h\tan(\theta_x)$ and $h\tan(\theta_y)$ account for possible beam tilt angles θ_x and θ_y for a simulation cell of height h.

The probe aperture function is defined as:

$$A(\mathbf{k}) = 1 \qquad \text{where } |\mathbf{k}| \leq k_{probe} \text{ and}$$
$$A(\mathbf{k}) = 0 \qquad \text{everywhere else.}$$

Once all coefficients are calculated, they are multiplied with the associated plane wave and summed over the whole cut out region defined by Equation (39) and the simulation is finished.

$$x_0 - \frac{d}{2f} \leq x \leq x_0 + \frac{d}{2f} \qquad \& \qquad y_0 - \frac{d}{2f} \leq y \leq y_0 + \frac{d}{2f} \qquad (39)$$

Ophus [23] stated that compared to the Multislice method the PRISM method will always be less accurate, but as long as the interpolation factor f is kept small, the error should be negligibly small. However, the speed up scales with f^4, making this method very useful for STEM simulations.

3 Experimental procedure

3.1 Samples

In this study, three different samples were used: a cantilever bending beam, a tensile and a cracked tensile specimen; each one of those was modeled using finite element methods. The material was chosen to be silicon. The advantage of silicon with its low ordinal number is that the electrostatic potential is smaller compared to heavier atoms, hence, the diffraction simulations should be more accurate [9].

3.2 Finite element calculations

For easier implementation and later evaluation, the isotropic orientation of the silicon unit cells was chosen in this thesis. The exact orientation of the crystal axis and the cartesian coordinate system can be seen in Figure 3, and the orthotropic constants for the finite element calculations are shown in Table 1.
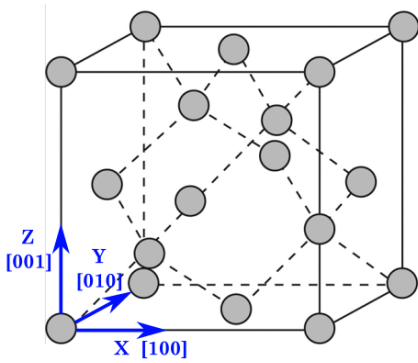
Table 1: *Silicon orthotropic constants for the orientation defined in Figure 3 [25,26].*

Orthotropic constants
$E_x = E_y = E_z = 130 \, GPa$
$G_{xy} = G_{yz} = G_{zx} = 79.6 \, GPa$
$v_{xy} = v_{yz} = v_{zx} = 0.28$

Figure 3: *Definition of the coordinate system in the silicon unit cell [24].*

The used mesh was chosen to be equivalent to the silicon unit cells, as that leads to an easy interpolation of the remaining atomic coordinates inside the unit cells. Therefore, cubic brick elements were used. The elements possess eight nodes in total, one at each corner and linear shape functions were used.

3.2.1 Cantilever bending beam

The shape of the cantilever bending beam is presented in Figure 4 with the exact dimensions in Table 2. The ratios of length to height and length to width were five to one, therefore the beam could be treated to be thin and the Euler-Bernoulli theory could be assumed [27,28]. The force application point was on the far right of the beam, with the direction of force in negative z-direction.
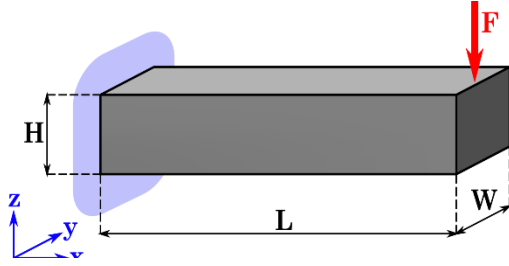
Figure 4: *Illustration of the bending beam.*

Table 2: *Dimensions of the cantilever bending beam.*

	# of elements	size [Å]
L	325	1765.0
W	65	353.0
H	65	353.0

3.2.2 Tensile specimen

For the tensile specimen, exactly the same dimensions as for the bending beam were used (Table 3). The force acted on the y-z-plane on the right in positive x-direction.
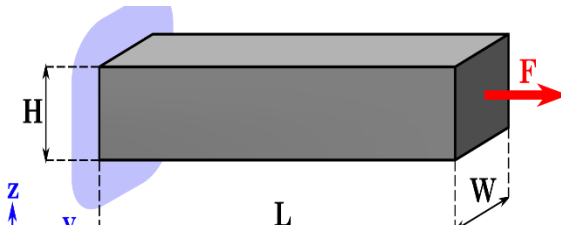
Figure 5: *Illustration of the tensile sample.*

Table 3: *Dimensions of the tensile specimen.*

	# of elements	size [Å]
L	325	1765.0
W	65	353.0
H	65	353.0

3.2.3 Cracked tensile specimen

For the cracked tensile specimen, the overall sample dimensions were reduced (Table 4) in order to extend the crack exactly to the middle in y-direction, as illustrated in Figure 6. The crack was implemented between the elements 160 and 161 in x-direction (L/2), from element 1 to 32 in y-direction (W/2) and over the whole height in z-direction (H). The crack tip was perfectly sharp, as no elements were removed.
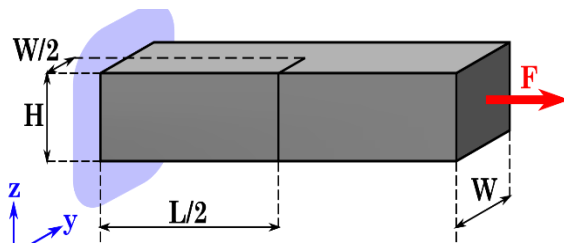
Figure 6: *Illustration of the cracked tensile specimen.*

Table 4: *Dimensions of the cracked tensile specimen.*

	# of elements	size [Å]
L	320	1738.0
W	64	367.6
H	64	347.6

3.3 Specimen preparation for PRISM

For the diffraction simulation, regions of 65 by 65 by 65 elements were taken from the finite element models. On the bending sample, three different regions were defined as illustrated in Figure 7. These samples are from now on referred to as

[13]

Bending I, Bending II and Bending III. In the case of the tensile specimen only one region was defined, equivalent to Bending I. In case of the cracked tensile sample again only one sample was defined, with a size of 64 by 64 by 64 elements centered around the crack tip.
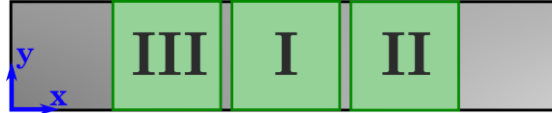
Figure 7: *Determination of the sample regions Bending I, II and III on the cantilever bending beam.*

As the bending samples were tilted out of the [001] zone axis, the three samples were rotated around the y-axis to align the [001] zone axis of the center element in x and y with the z-axis as schematically shown in Figure 8 below. This step was not necessary for the tensile and cracked tensile specimens.
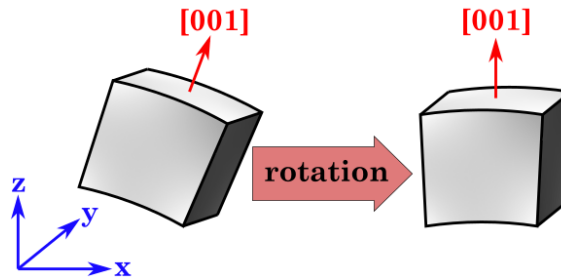
Figure 8: *Illustration of the rotation of the bending samples. The samples were rotated around the y-axis to align the [001] zone axis in the middle of the x-y-plane with the z-axis.*

Subsequently, the positions of the remaining atoms in each unit cell had to be calculated. This was achieved utilizing the linear shape functions of a cubic brick element and the nodal displacements of the corner points of each element.

Having interpolated all remaining atom positions, the input file for the diffraction simulation was created. PRISM requires an atomic coordinate file with a special structure, as specified on the website [29]. The occupancy probability of each lattice site was set to 100 %, and to account for thermal diffuse scattering a Debye-Waller-factor of 0.076 Å [30] was used. Further, the supercell dimensions in x- and y-direction were set to be equal in order to obtain diffraction images with the same number of pixels in both directions.

In addition, an unstrained reference sample and a perfectly strained sample were created, as to determine the precision and accuracy of the strain measurements. The perfectly strained sample was strained by 2.00 % in x-direction and -0.56 % in y- and z-direction according to Poissons ratio, and no shear was introduced.

3.4 PRISM – diffraction simulation

The diffraction simulation was carried out using the simulation program PRISMATIC [23,31]. The parameters for the simulation are shwon below in Table 5 and an illustration of the diffraction setup is shown in Figure 9.

Table 5: *Parameters used for the STEM simulation.*

Pixel size	0.2 A		Δz	1,35 Å
U	200 kV		f	2
α	2.0 mrad		Probe step	5.43 Å
α_{max}	3.0 mrad		Probe tilt	0.0
C1, C3, C5	0.0, 0.0, 0.0			

The pixel size needed to be chosen small enough, as otherwise forbidden diffraction spots appeared visible, which came with the drawback of longer computation times. The probe semi-angle alpha was set to 2 mrad in accordance with typical experimental ones. For simplicity, the aberrations were all set to zero. The slice thickness Δz was chosen to be the mean atomic distance along the z-axis, as 1 to 2 Å should be sufficient for most cases [32].

The scan range was set from 0.15 % to 0.85 % in both x- and y-direction of the sample, leading to a scan area of roughly 247 by 247 Å². In order to calculate roughly one diffraction image per unit cell, the step size was set to 5.43 Å. These settings resulted in 46 by 46 diffraction images per experiment. In principle, higher values of the interpolation factor f lead to drastically lower computation times. However, the number of pixels in the final diffraction image is inversely proportional to f. Hence, f was set to 2 in order to achieve diffraction images with a sufficient resolution of 440 by 440 pixels. Due to the long computation times, only one frozen phonon configuration was calculated.
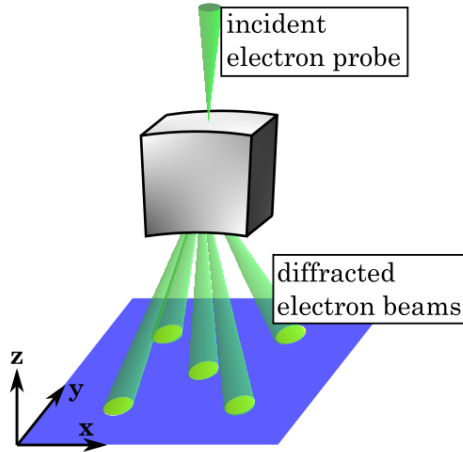
Figure 9: *Setup of the diffraction simulation. The incident electron probe is parallel to the z-axis.*

[15]

3.5 Strain measurement

The strain evaluation from the diffraction images was carried out in Gatan Digital Micrograph using the square-root magnitude weighted phase correlation. This should provide better results compared to standard techniques such as cross correlation methods, especially since the intensity distribution inside the disks is pronounced [33]. Only the {220} disks were used for the evaluation, as the intensity of the {400} disks was at times too low to be properly detected.

3.6 Strain calculation from FE-Data

In order to compare the measured strains from the evaluation of the diffraction images, the strains ϵ_{xx}, ϵ_{yy} and ϵ_{xy} of the finite element model were calculated. The calculation of the strains is illustrated in Figure 10. One element is taken from the FE mesh with the three points of interest P_1, P_2 and P_3 and their corresponding nodal displacement vectors $\overline{u_\iota}$, defined by Equations (40-42). The strains can then be calculated using Equations (43-45).
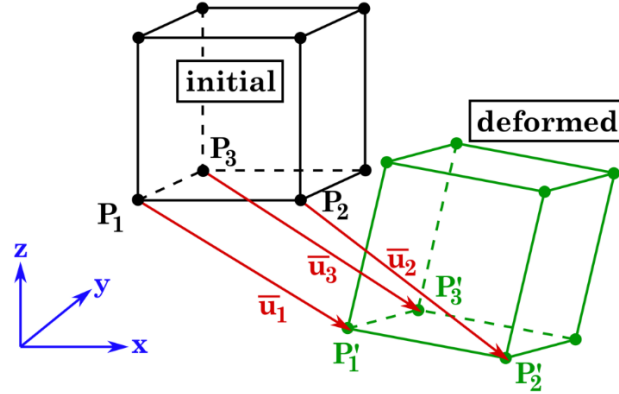
Figure 10: *Definition of the points of interest for the calculation the strains in one element. The red vectors define the nodal displacement of the given point due to the deformation.*

$$\overrightarrow{u_1} = P'_1 - P_1 = \begin{pmatrix} x'_1 - x_1 \\ y'_1 - y_1 \\ z'_1 - z_1 \end{pmatrix} = \begin{pmatrix} u_{1x} \\ u_{1y} \\ u_{1z} \end{pmatrix} \tag{40}$$

$$\overrightarrow{u_2} = P'_2 - P_2 = \begin{pmatrix} x'_2 - x_2 \\ y'_2 - y_2 \\ z'_2 - z_2 \end{pmatrix} = \begin{pmatrix} u_{2x} \\ u_{2y} \\ u_{2z} \end{pmatrix} \tag{41}$$

$$\overrightarrow{u_3} = P'_3 - P_3 = \begin{pmatrix} x'_3 - x_3 \\ y'_3 - y_3 \\ z'_3 - z_3 \end{pmatrix} = \begin{pmatrix} u_{3x} \\ u_{3y} \\ u_{3z} \end{pmatrix} \tag{42}$$

$$\epsilon_{xx} = \frac{\partial u_x}{\partial x} \approx \frac{\Delta u_x}{\Delta x} = \frac{u_{2x} - u_{1x}}{x_2 - x_1} \tag{43}$$

$$\epsilon_{yy} = \frac{\partial u_y}{\partial y} \approx \frac{\Delta u_y}{\Delta y} = \frac{u_{3y} - u_{1y}}{y_3 - y_1} \tag{44}$$

$$\epsilon_{yx} = \epsilon_{xy} = \frac{1}{2}\left(\frac{\partial u_y}{\partial x} + \frac{\partial u_x}{\partial y}\right) \approx \frac{1}{2}\left(\frac{\Delta u_y}{\Delta x} + \frac{\Delta u_y}{\Delta x}\right) = \frac{1}{2}\left(\frac{u_{2y} - u_{1y}}{x_2 - x_1} + \frac{u_{3x} - u_{1x}}{y_3 - y_1}\right) \tag{45}$$

The resulting strain distribution was further smoothed as the calculated strains showed some significant spikes in areas where a steady course was expected. The smoothing was carried out using a rectangular function in the x-y-plane. In Figure 11 the scheme of the smoothing for the strains in the red node is shown, with the boundaries of the smoothing function for the individual specimens. For the bending beam and the tensile sample 25 nodes were used for smoothing, in favor of a smoother course, as the gradient should be linear. The cracked tensile sample however shows significant strain gradients, especially in the area round the crack tip. To distort this gradient as little as possible, only nine elements were used for the smoothing. The smoothed strains were then compared to the strain ϵ_{xx} which was provided directly from the FEA to ensure that the smoothing was successful.
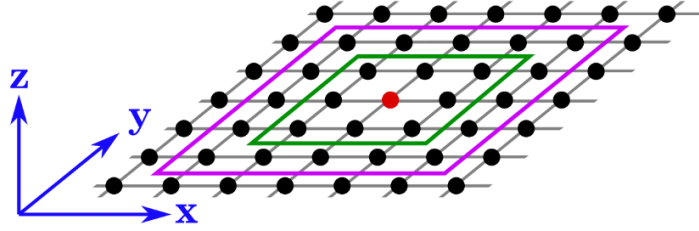
Figure 11: *Illustration of the smoothing process. To smooth the strain value in the red node, the mean strain of all nodes enveloped by the purple square for the bending and tensile specimen were used. For the cracked tensile sample only the nodes inside the green square were used.*

4   Results and discussion

In this section the results obtained from the NBED-simulations are presented. First, the precision and accuracy of the strain measurement technique are determined using the reference sample and the ideal tension sample. Second, the bending beam followed by the tensile and crack tensile specimens are analyzed and compared.

4.1   Precision σ and accuracy Δ of the simulations
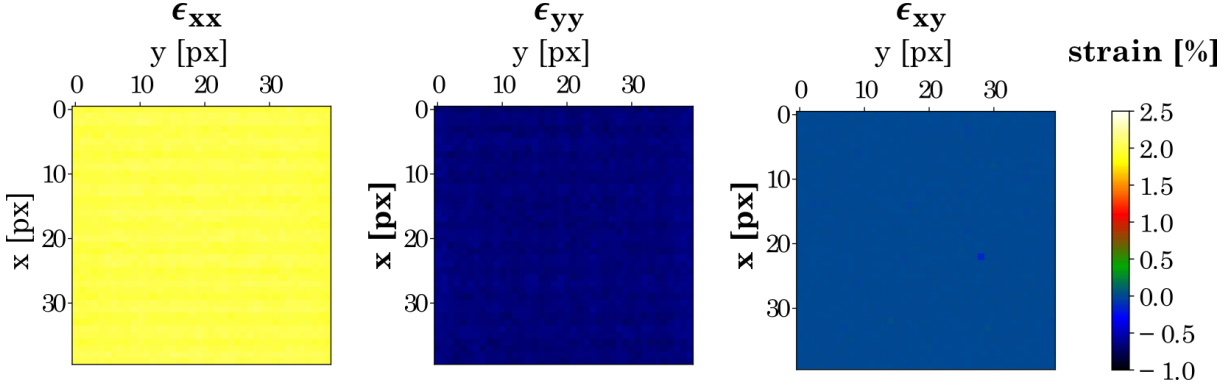
Figure 12: *Strain maps obtained from the ideal tensile sample. a) shows the strain ϵ_{xx}, b) the strain ϵ_{yy} and c) the strain ϵ_{xy}. The colorbar on the right is valid for all three figures.*

Figure 12 shows the strain maps obtained from the ideal tension sample. The results show only small deviations over the whole scan region, leading to the assumption that both the diffraction simulation and the disk registration work properly. The measured strains compare quite good with the actual strain state of the sample. To further quantify the results, histograms for each strain direction were created and are presented in Figure 13a to c, together with the real strain value in the sample (indicated by the purple lines). It should be noted that the strain in the histograms is unitless and therefore two orders of magnitude smaller than in the strain maps. This will be the case for all the following histograms. The bin size of the histograms was set to $5 \cdot 10^{-5}$.

Figure 13a shows that the mean measured strain ϵ_{xx} is +2.009 % with an accuracy Δ_{xx} of +0.009 % and a precision σ_{xx} of 0.031 %. Interestingly, the results for the strain along the y-direction show a significantly worse accuracy but the precision is comparable (Figure 13b). The measured mean strain ϵ_{yy} is 0.668 % with an accuracy Δ_{yy} of -0.108 % and a precision σ_{yy} of 0.021 %. Figure 13c shows that the mean measured strain ϵ_{xy} is +0.001 % with Δ_{xy} = +0.001 % and σ_{xy}= 0.009%. Values for precision found in literature range from around 0.06% to 0.12 % [34–37] and for accuracy from 0.06 % to 0.1 % [35,37,38]. The here obtained values for both,

[18]

precision and accuracy, are in the same order of magnitude or even significantly lower, thus the simulations can be assumed to be accurate and the chosen parameters for the diffraction simulation as adequate.

Figure 13d shows an exemplary diffraction image of the ideal tension sample. The image shows only the allowed (000), {220} and {400} diffraction disks. However, it can be seen that the {400} spots have very low intensity, comparable to the background noise. Inside each diffraction disk, a strong intensity distribution due to dynamical diffraction is visible.
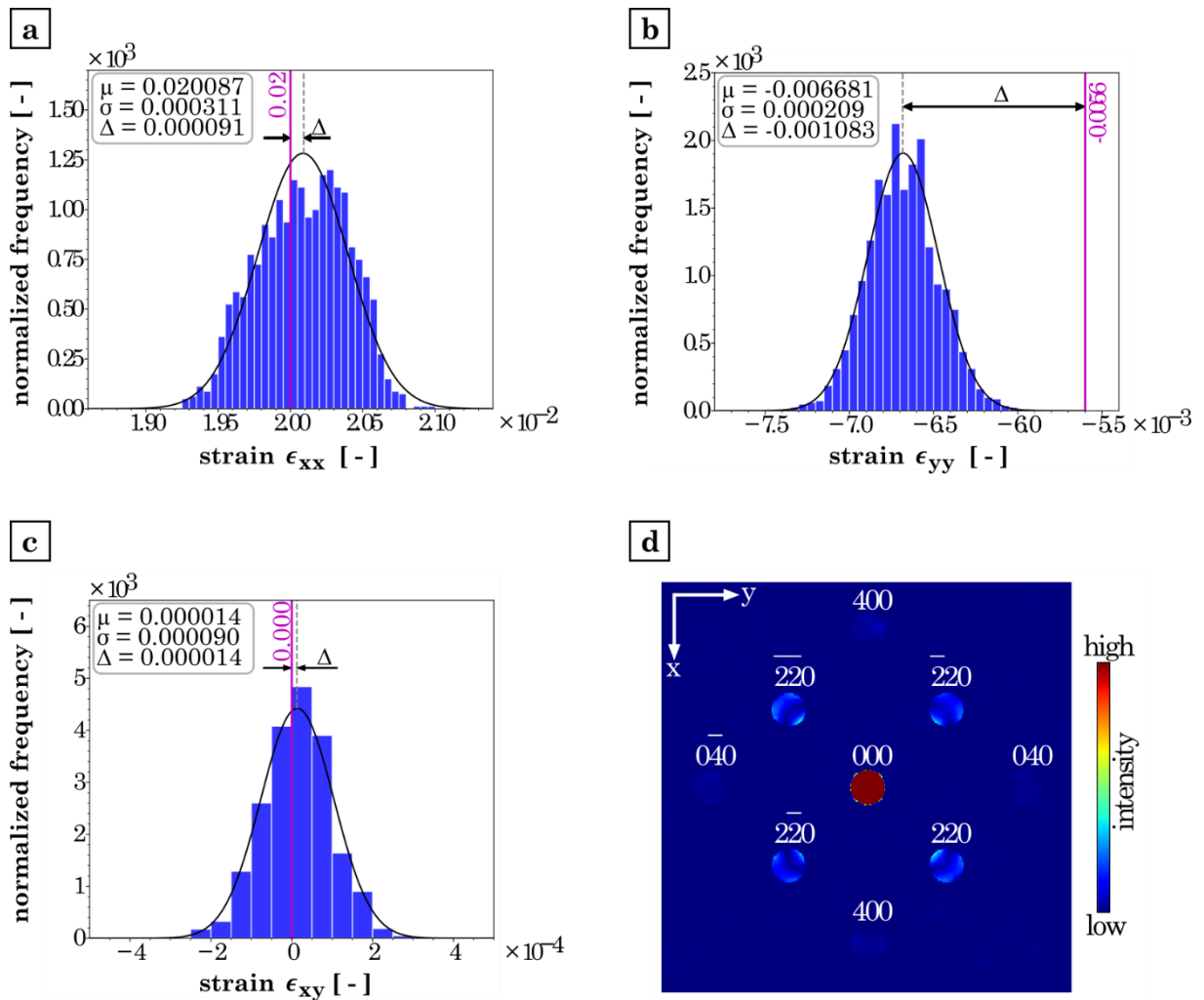
Figure 13: *Results of the histogram analysis of the strains measured from the ideally strained tensile specimen. a) the strain ϵ_{xx}, a) the strain ϵ_{yy} and c) the strain ϵ_{xy}. d) shows an exemplary diffraction image including the indexing of the disks.*

4.2 Cantilever bending beam

Three sample regions on the cantilever bending beam are analyzed regarding their strain distribution. For the sake of better comparability between the three tests, the results of each strain direction are directly compared, rather than presenting each sample individually.

4.2.1 Cantilever bending beam - ϵ_{xx}

Figure 14 shows the comparison between the measured strain ϵ_{xx} and the arithmetic mean strain obtained from the finite element simulation, which is the predicted result of the strain mapping according to [39,40], for all three sample regions. The results of Bending I in Figure 14a show positive strain values in the range of 0.0 to 0.1 % over the whole sample region, whereas the arithmetic mean strain of the FEA is 0.000 % with a negligible standard deviation of only 0.001 % (Figure 14b). Overall, the strain distribution appears to be quite homogenous, however, in the top third the strain shows slightly higher values.

In general, the same holds true for Bending II as can be seen in Figures 14c and d. The strain map looks nearly the same as the one of Bending I. However, the strain values are smaller as gentle green areas (respectively slightly negative strains) already appear visible. On the top border (x → 0), the strain values slightly increase to values around 0.1 % which is comparable to the rise in the top third in Figure 14a.

The appearance of the strain map obtained from Bending III (Figures 14e and f) indicates that the strain distribution inside the sample is very inhomogeneous. In the middle region the measured strain shows similar result as compared to the other two samples. At the boundaries in x direction, the measured strain drops significantly, showing values as low as -0.2 %. This is in great contrast to the other two samples, where the strain appeared to rise at the edges. In y-direction, the same kind of drop can be seen but is less pronounced, as the strain drops only to around -0.1 %. Similar to the two samples before, a rise in the strain in the top half can be seen, with strain values up to around 0.1 %

To further quantify the results, strain profiles along the x- and y-axis were created and are shown in Figure 15. Each graph includes three profiles: one from the middle (index 23) and two from each side (index 10 and 35). The black graphs indicate the outer fiber strains in both the tensile (top layer) and compression (bottom layer) areas of the samples.
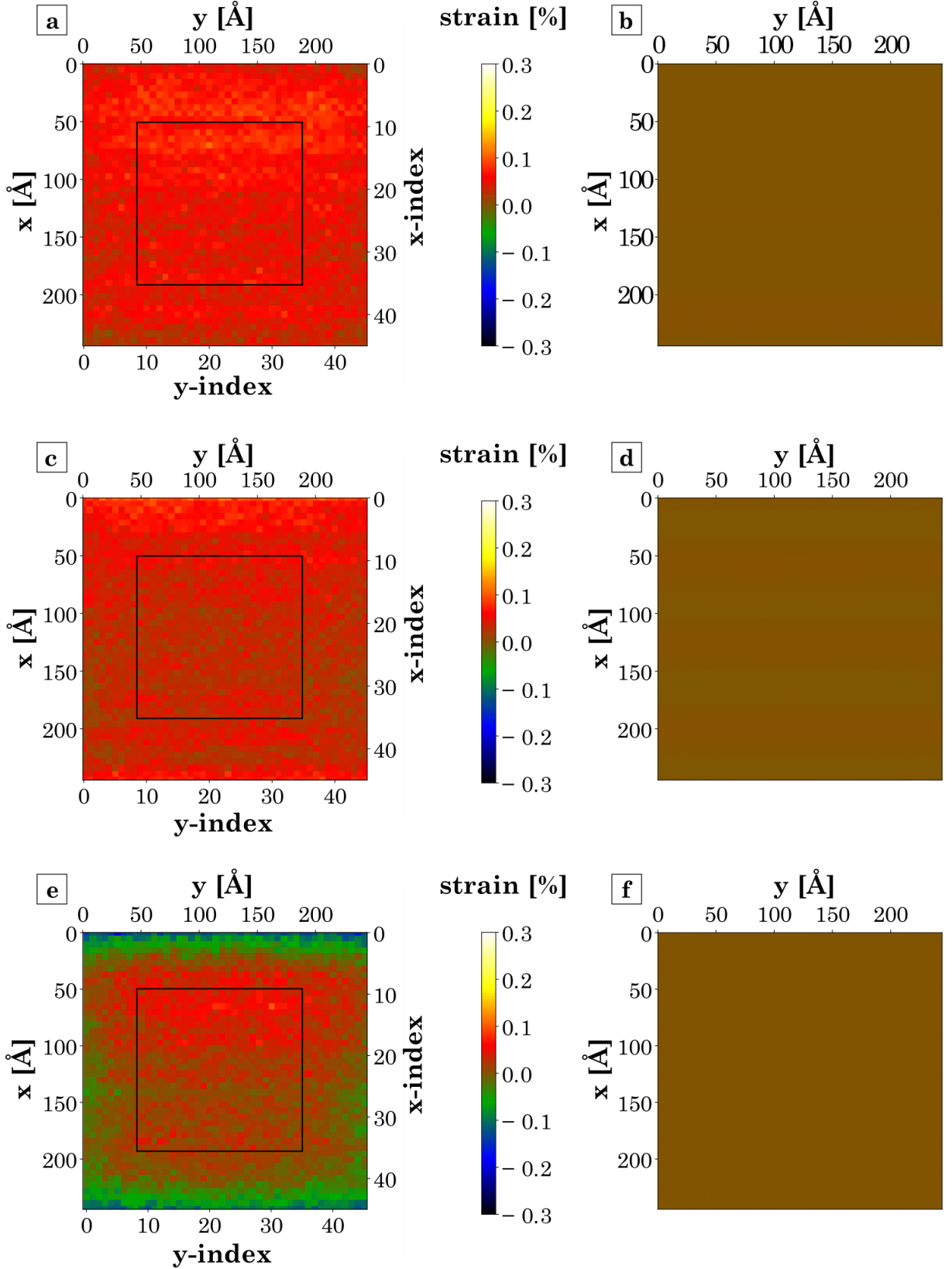
Figure 14: *Comparison between the ϵ_{xx} strain maps (left column) and the arithmetic mean strain ϵ_{xx} along the electron beam direction obtained from the FEA (right column). a) and b) results of Bending I, c) and d) from Bending II and e) and f) from Bending III.*
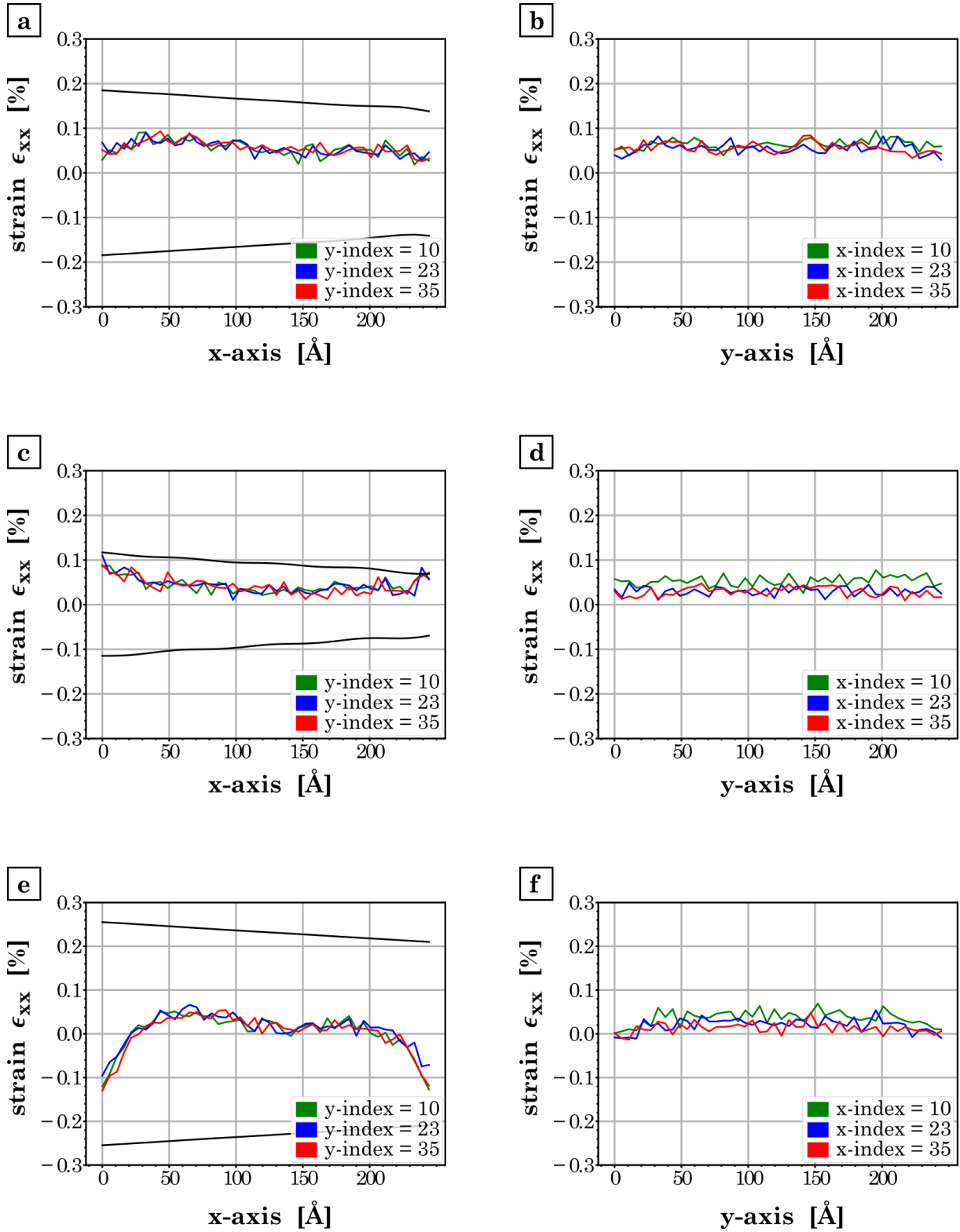
Figure 15: ϵ_{xx} *strain profiles of three bending samples along the x- and y-axis. a) strain profile of Bending I along the x-axis and b) along the y-axis. c) strain profile of Bending II along the x-axis and d) along the y-axis. e) strain profile of Bending III along the x-axis and f) along the y-axis. The indices of the used strain can be seen in Figure 14.*

Figures 15a to f indicate that the measured strain does indeed compare quite good with the arithmetic mean strain along the electron beam direction. However, the results are not constant over the whole scan region. First, the strain shows some deviations from scan point to scan point. This is the typical measurement error from the nano diffraction image analysis, originating from errors like disk registration. Furthermore, the Bending I sample shows an increase of around 0.05 % between 0 and 40 Å in x-direction in Figure 15a. This increase is even more pronounced in the sample Bending III (Figure 15e), where the strain level drops from around 0.05%, down to values lower than -0.10%. Additionally, towards the right edge the strain level shows a decrease in the same manner. This phenomenon is most likely caused by the bending of the sample. The fact that the sample is bent around the y-axis results in an angular deviation between the [001] zone axis and the microscope optical axis, referred to as beam tilt, respectively specimen tilt in this present case. This angular deviation causes excitation of specific diffraction spots, leading to evaluation error in the strain analysis [33]. This topic will be further discussed in Section 4.2.4. Interestingly, in case of the least bent sample, Bending II, this phenomenon cannot be seen, but rather the measured strain rises at the edges (Figure 15c).

The strain profiles along the y-axis (Figure 15b, d and f) show no particular abnormalities. The strains are nearly constant over the whole range and deviate only in the range of the measurement precision σ as determined in Section 4.1. (The outer fiber strains are not included for better clarity, as each profile has different outer fiber strains.)

To quantify the precision and accuracy of the measured strains, histograms for all three samples have been calculated and are shown in Figure 16a to c. To reduce the influence of the strain deviations at the boundaries, only the values inside the black rectangle in Figure 14a, c and e were used for this analysis. The measured precisions range from 0.011 % to 0.018 % and are again in good agreement with values mentioned in literature [34–36], confirming that the simulations are accurate.

The average measured strains are +0.058 % for Bending I, +0.035 % for Bending II and +0.027 % for Bending III proving that the measured strain is in fact comparable to the real average strain along the beam direction but not equal. However, taking the outer fiber strains into account, no direct correlation between measured strain and maximum outer fiber strain in the sample could be found. The fact that the measured mean strain is positive for all three samples leads to

two possible explanations. First, the diffraction simulation might be more sensitive to positive strains than negative ones. Second, the fact that the electron beam penetrates the sample in the tension region first has an impact on the measured strain. This second possible reason is further strengthened by the fact that the electron probe was focused on the top layer. However, due to the small probe semi convergence angle of only 2 mrad, this should only have a minor influence on the result.

It should also be noted that the measured strains are all of same magnitude as the accuracy of the measurement. Therefore, even small deviations can lead to false assumptions. However, the fact that all three samples showed comparable results confirms that the simulations are accurate.
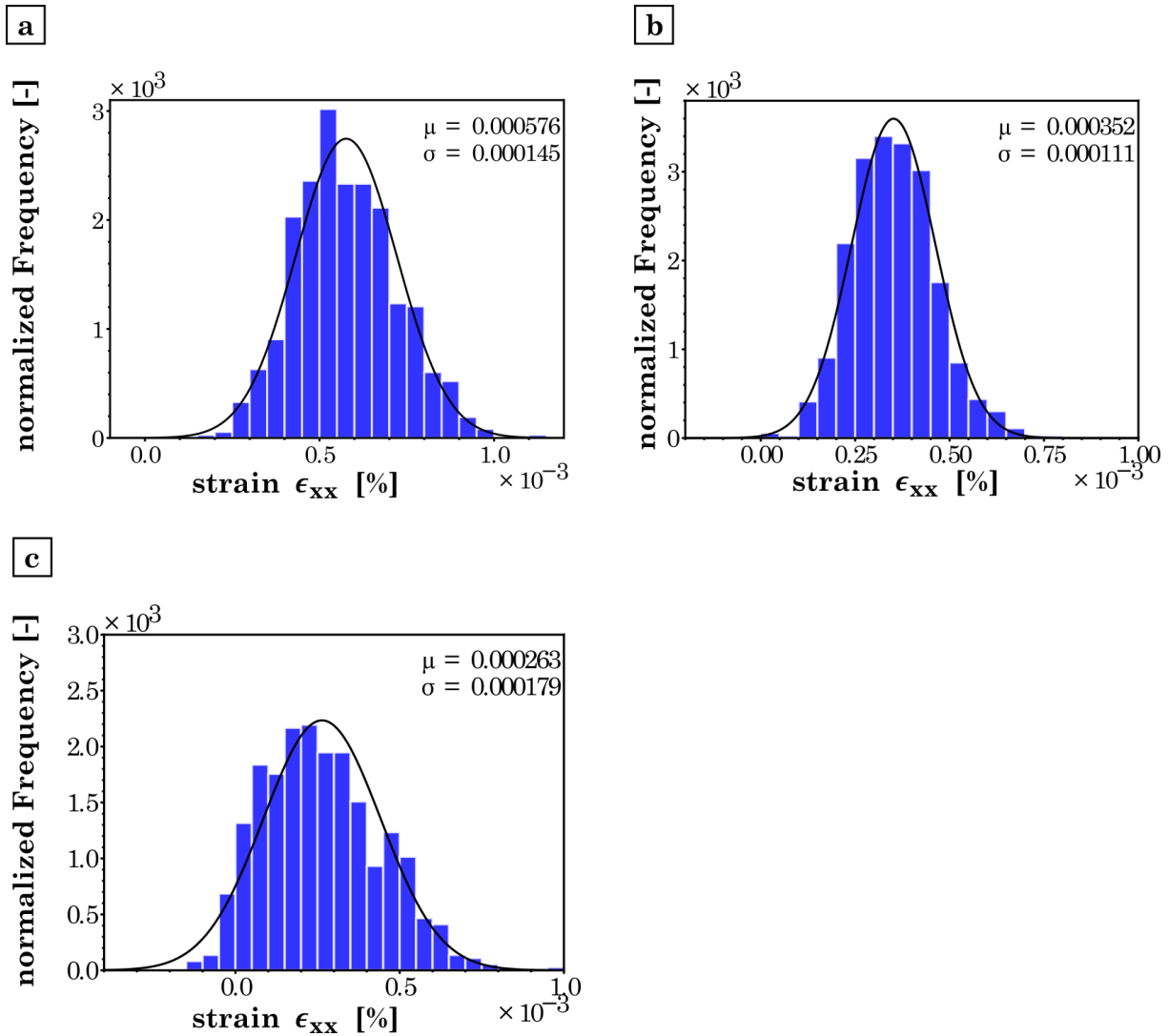
Figure 16: *Histogram analysis of the measured strains ϵ_{xx} for a) Bending I, b) Bending II and c) Bending III.*

[24]

4.2.2 Cantilever bending beam - ϵ_{yy}

Due to the lateral contraction, the ϵ_{yy} strain gradient along the microscope optical axis is reversed compared to ϵ_{xx}. The electrons enter the compression area of the sample and leave through the tensile area. The examination of the measured strain in y-direction should therefore provide valuable insight into the averaging of the diffraction angle.

First the strain maps are analyzed and again compared to the arithmetic mean strain along the electron beam direction (Figure 17). In case of the samples Bending I and II, the measured strain in the middle region is close to zero, with some minor deviations in both negative and positive direction (Figures 17a and c), but overall being in very good agreement with the expected result from the FEA (Figures 17b and d). In contrast, the middle region of Bending III shows mostly green areas equivalent to strain values between -0.1 and 0.0 %.

Bending I shows a decrease of about -0.1 % in the measured strain at the boundaries in x-direction, where bright green areas are visible. This characteristic is also present in for Bending III, where the strain drops from around -0.1 % to values as low as -0.2 %. However, no such event is observable at the sample with the lowest outer fiber strain, Bending II. This effect is comparable to the one described in Section 4.2.1 and can also be traced back to the excitation of diffraction disks. Again, this will be treated in more detail in Section 4.2.4.

Furthermore, all three maps (Figures 17a, c and e) show a rise in the measured strain at the edges in y-direction, where vibrant red areas are visible. This phenomenon is most pronounced for Bending II, where it is present over the whole range in x-direction. In the case of Bending I, this rise is visible nearly over the whole x-range but appears to be weakened at the top and bottom, where it overlays with the decreased strain described in the paragraph above. In the same manner, but far more pronounced, this is also visible in the map of Bending III, where the rise in strain is only visible between the x-indices 12 to 33.

[25]
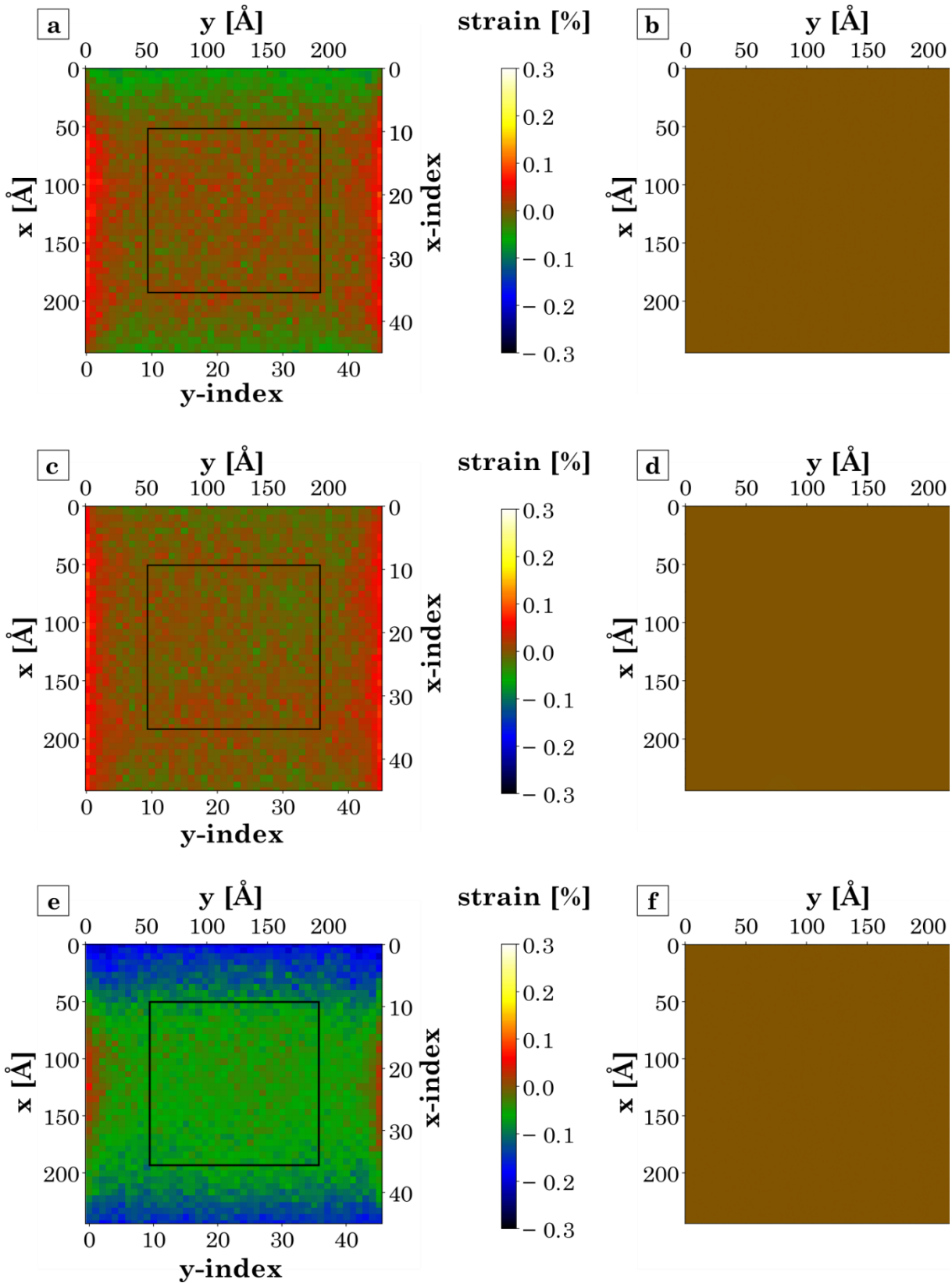
Figure 17: *Comparison between the ϵ_{yy} strain maps (left column) and the arithmetic mean strain ϵ_{yy} along the electron beam direction obtained from the FEA (right column). a) and b) results of Bending I, c) and d) from Bending II and e) and f) from Bending III.*

[26]
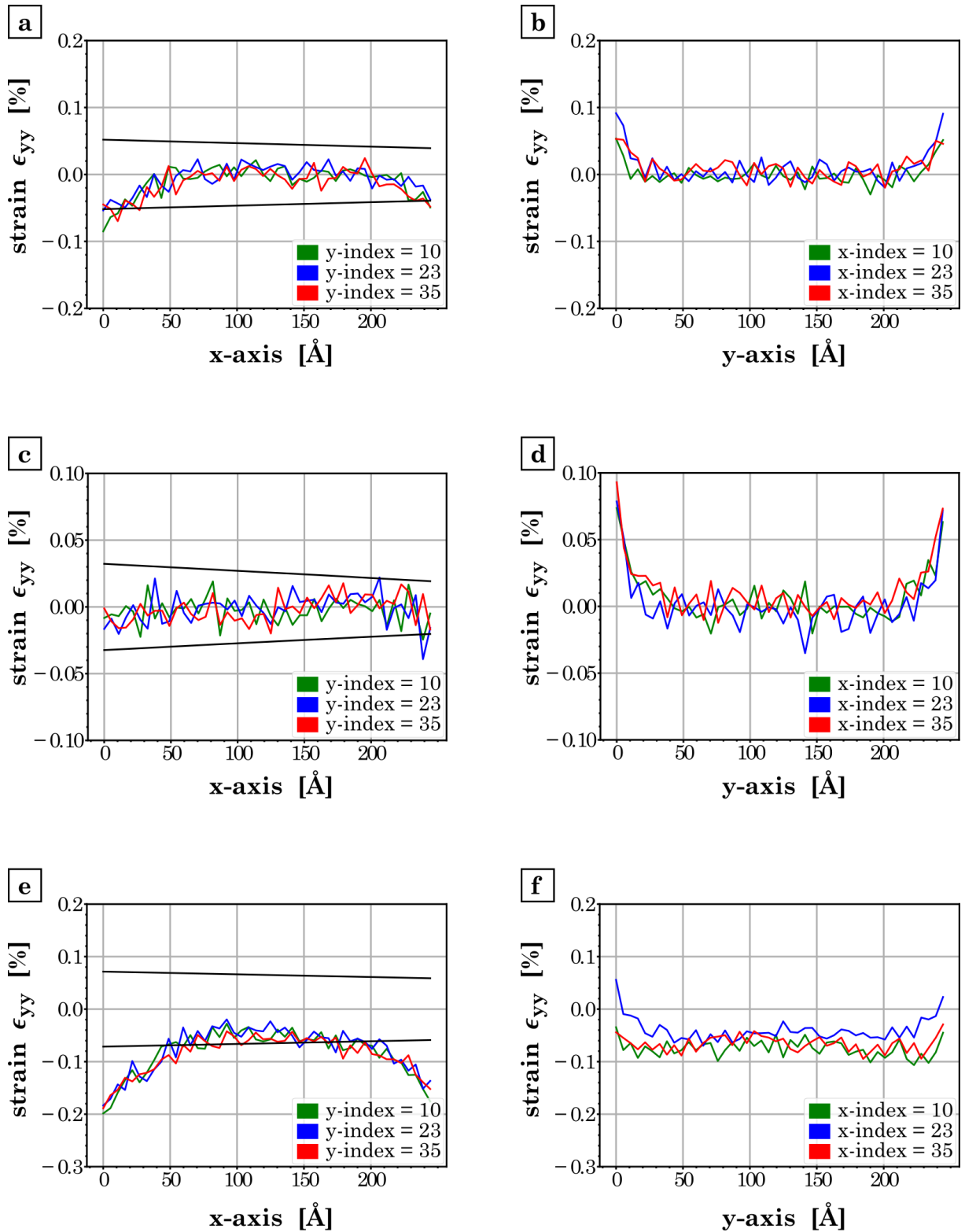
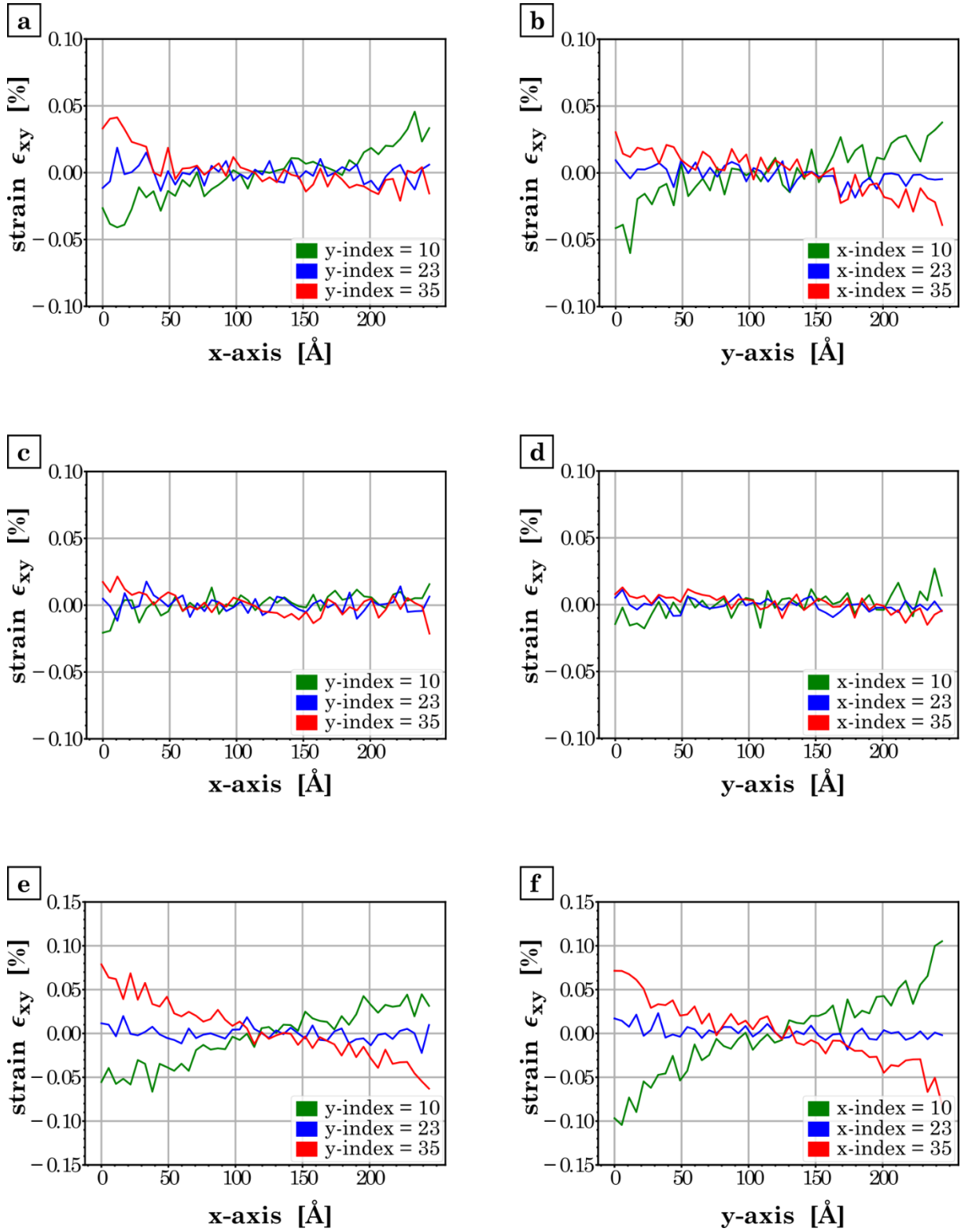**Figure 18:** ϵ_{yy} *strain profiles of three bending samples along the x- and y-axis. a) Strain profile of Bending I along the x-axis and b) along the y-axis. c) Strain profile of Bending II along the x-axis and d) along the y-axis. e) Strain profile of Bending III along the x-axis and f) along the y-axis. The indices of the used strain values can be seen in Figure 17.*

For further visualization of the results, strain profiles along both axes were created and are presented in Figure 18.

The graphs for Bending I and II (Figure 18a and c) show that the measured strain in the middle region is almost zero, deviating only by the usual measurement precision, perfectly reflecting the average strain from the FEA. Figure 18e shows that for the highest outer fiber strain, the measured strain is negative even in the middle region where the least errors in the diffraction simulation are expected. As the outer fiber strain is the highest for this sample, the influence of the direction of the incident electron beam on the averaged strain should be the strongest here.

To investigate the influence of whether the imaging electrons enter the compressive or tensile region first, ϵ_{yy} of Bending III and ϵ_{xx} of Bending II are compared as the magnitudes of the outer fiber strains are best comparable (ϵ_{yy} = 0.7 % compared to ϵ_{xx} = 0.9 % at x-index = 23). While the strain analysis for Bending II resulted in a positive strain value, the analysis for Bending III provided a negative value in the same magnitude. This strengthens the assumption that the measured strain depends on whether the imaging electrons first enter the tensile or compression region of the sample. Apparently, this effect cannot be detected in the other two samples, making a final conclusion impossible.

As already mentioned, the strain level in both Bending I and III decreases at the edges from around 0.0 % to -0.07%, respectively from-0.05 % to -0.2 % in Figures 18a and c, which can again be traced back to the angular deviation between the zone axis and the microscope optical axis.

The three strain curves along the y-axis all show the same characteristics. The strain in the middle region is constant neglecting the usual measurement errors. At the edges, the strain levels rise to about 0.1 % in all three graphs. Further discussion on this follows in Section 4.2.4.

The histogram analysis (Figure 19) brought to light that the average strains ϵ_{yy} measured for the three samples are:

- Bending I: $\epsilon_{yy} = \quad 0.002 \pm 0.011$ %
- Bending II: $\epsilon_{yy} = \quad 0.002 \pm 0.010$ %
- Bending III: $\epsilon_{yy} = -\ 0.054 \pm 0.014$ %

The simulations are accurate, as the precisions of all three tests are about one order of magnitude smaller compared to values found in literature.
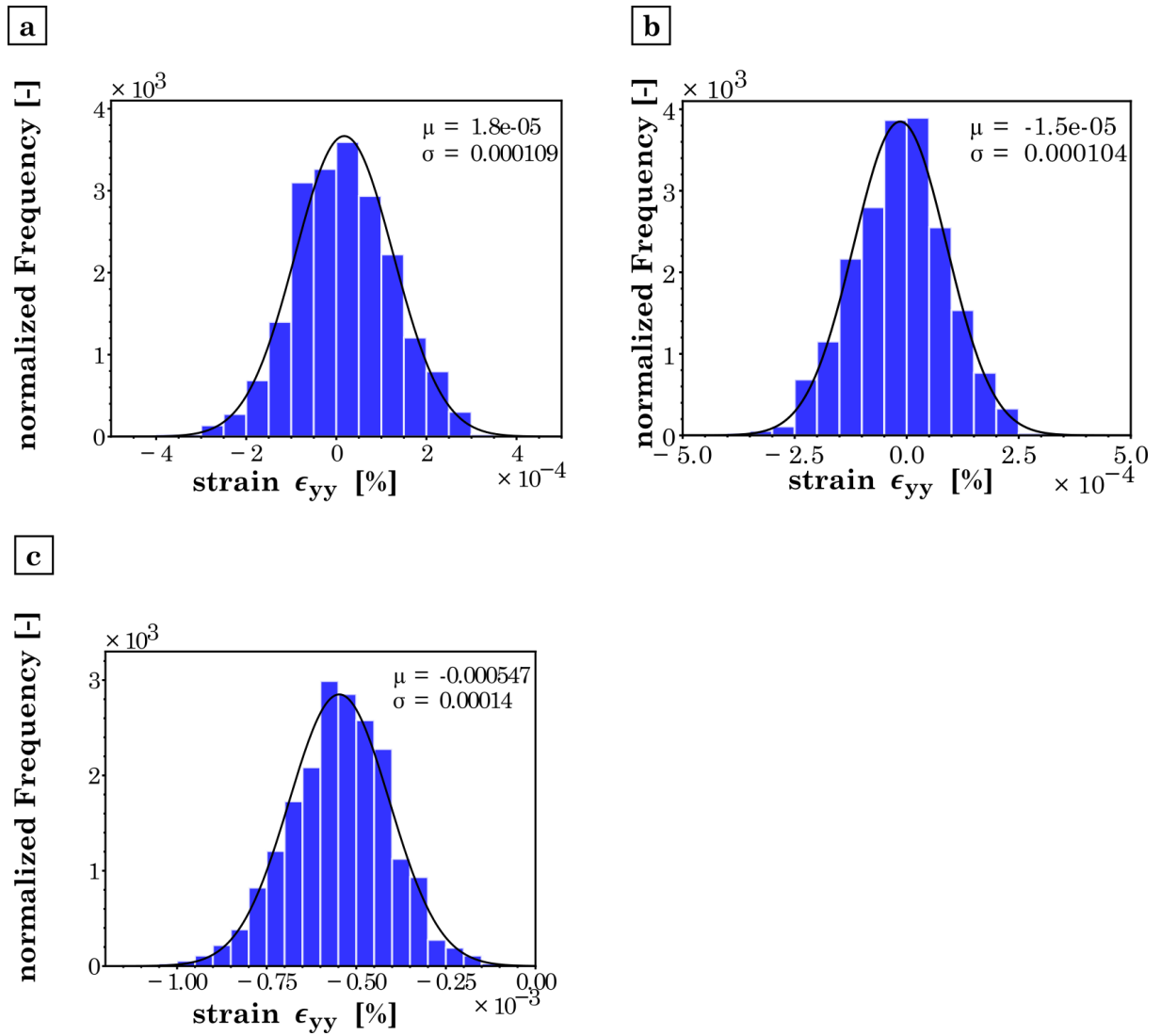
Figure 19: *Histogram analysis of the measured strains ϵ_{yy} for a) Bending I, b) Bending II and c) Bending III.*

.

4.2.3 Cantilever bending beam - ϵ_{xy}
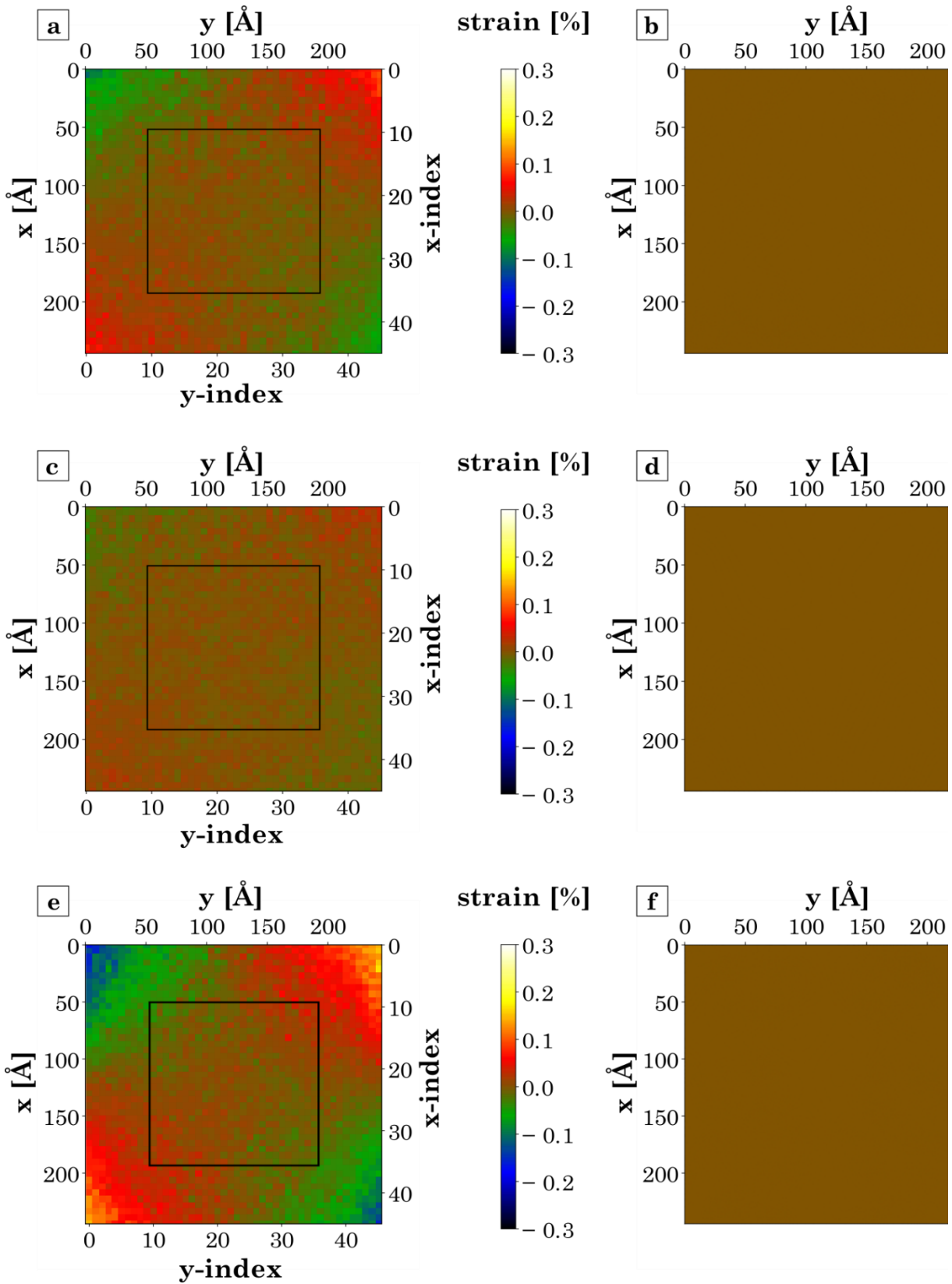
Figure 20: *Comparison between the ϵ_{xy} strain maps (left column) and the arithmetic mean strain ϵ_{xy} along the electron beam direction obtained from the FEA (right column). a) and b) results of Bending I, c) and d) from Bending II and e) and f) from Bending III.*

[30]

Lastly, the obtained maps of ϵ_{xy} are compared and analyzed. According to the finite element analyses the strains ϵ_{xy} are zero over the whole sample regions and also along the electron beam axis. This is a direct consequence of the bending beam being thin and hence, the Euler-Bernoulli theory holding true. Consequently, no significant characteristics in are expected.

The comparisons between the measurements and the FEA in Figure 20 point out that in the middle regions of the scan areas the measured strain is indeed zero, again neglecting the usual measurement errors. Towards the corners, however, the measurements show results completely differing from the expected value. In all three samples (Figures 20a, c and e) the shear strain rises from the middle region towards the upper right and lower left corners. A direct correlation between the magnitude of this rise and the magnitude of the bend can be observed. In the other two corners of each map, the measured strain drops to negative strain values but shows a similar correlation. To further visualize this correlation, strain profiles along both axes were created and are presented in Figure 21.

The three graphs in Figure 21a confirm the impression given by the strain maps that the strain rises more or less linear towards the corners. The blue graph is obtained from y-index 23 where no rise in the strain can be determined. For smaller y-indices (represented by the green graph in Figure 21a) the strain rises consistently along the x-axis. For y-indices greater than 23 (represented by the red graph) the curve drops along the x-axis. The overall course and maximum strain values of both the green and red graph are in good agreement. Figures 21c and e basically show the same result. As the bend in Figure 21c is less compared to Figure 21a, this characteristic is less pronounced. In Figure 21e the gradient is more pronounced due to the stronger bend in this sample.

The strain graphs along the y-axis (Figure 21b, d and f) show the same behavior as the ones along the x-axis.

[31]

Figure 21: ϵ_{xy} *strain profiles of three bending samples along the x- and y-axis. a) Strain profile of Bending I along the x-axis and b) along the y-axis. c) Strain profile of Bending II along the x-axis and d) along the y-axis. e) Strain profile of Bending III along the x-axis and f) along the y-axis. The indices of the used strain can be seen in Figure 20.*

[32]

To quantify the measured strains in the three samples, a histogram analysis was carried out. The outcomes, presented in Figure 22, prove that the determination of ϵ_{xy} inside the rectangular areas indicated in Figures 20a, c and e is in fact measured to be zero. The results are:

- Bending I: $\epsilon_{xy} = 0.000 \pm 0.008\,\%$
- Bending II: $\epsilon_{xy} = 0.001 \pm 0.005\,\%$
- Bending III: $\epsilon_{xy} = 0.001 \pm 0.012\,\%$

The determined accuracies of these experiments are extremely good und up to two orders of magnitude lower compared to experimental values.
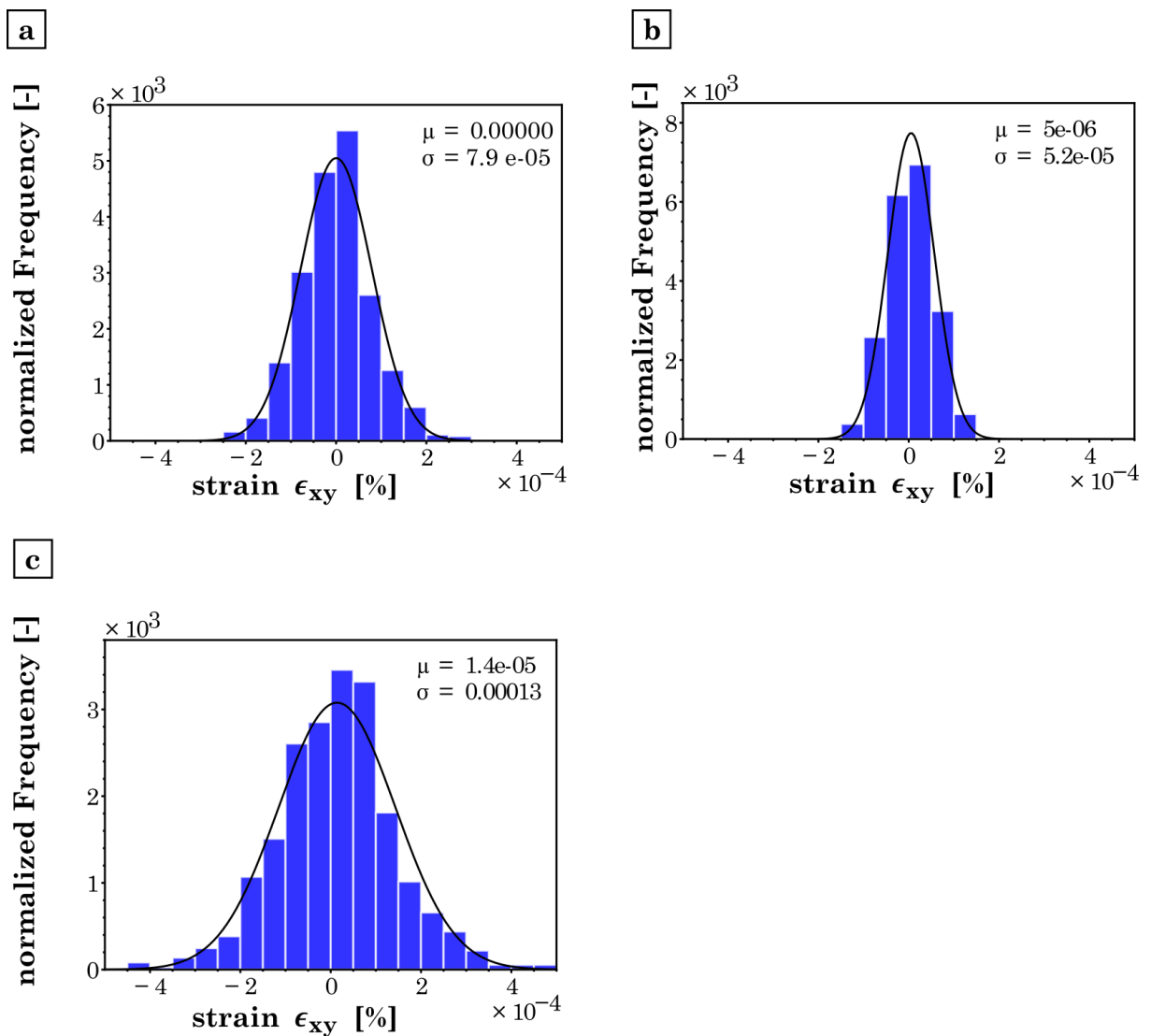
Figure 22: *Histogram analysis of the ϵ_{xy} maps from a) Bending I, b) Bending II and c) Bending III.*

4.2.4 Influence of specimen tilt

In this section, the influence of specimen tilt on the diffraction images and further on the measured strains is analyzed.

Due to the bend of the specimen, the [001] zone axis is not equal to the microscope optical axis over the whole sample. Consequently, some diffraction spots get excited, leading to drastically higher intensities, which makes the peak finding process more prone to errors [41]. The influence of the direction of the angular deviation on the diffraction images and measured strain will therefore be analyzed. The angular deviation angle is defined as the angle the zone axis is tilted away from the optical axis. For the analysis, the total angular deviation is split into two rotational parts, β around the x-axis and γ around the y-axis. The directions of the angles β and γ and the sign convention are defined in Figure 23 below.
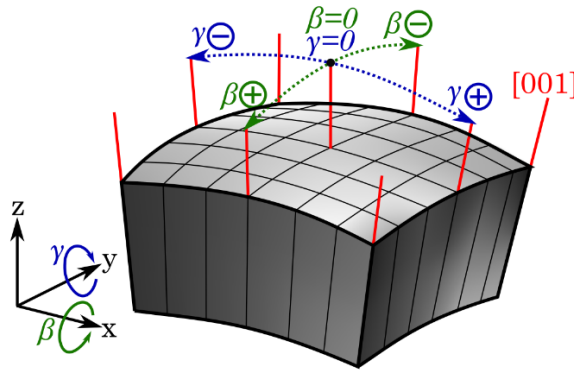
Figure 23: *Definition of the two angular deviation angles β and γ between the [001] zone axis and the microscope optical axis and the sign convention.*

The analysis here will be based on specimen Bending III, as the effects should be most pronounced for the strongest bend. The angular deviation γ ranges from -1.7 to +1.6 mrad and β from -0.46 to +0.45 mrad, respectively.

In Figure 24 nine exemplary diffraction images are presented, where the {400} spots were cut off as they were not used in the evaluation. Figure 24e shows the diffraction image obtained from the middle region of the sample, where both β and γ are zero. The intensities of all four {220} disks are well comparable and all possess equal intensity distributions inside the disks. For a negative tilt angle γ and no tilt in β the $2\bar{2}0$ and 220 spots are strongly excited, especially in regions closest to the central spot, but also the $\bar{2}\bar{2}0$ and $\bar{2}20$ disks appear slightly excited (Figure 24b). The strong excitation of these two disks led to an underestimation of both ϵ_{xx} and ϵ_{yy} by 0.1 to 0.2 %. The measurement of ϵ_{xy} was, however, not affected by this tilt.
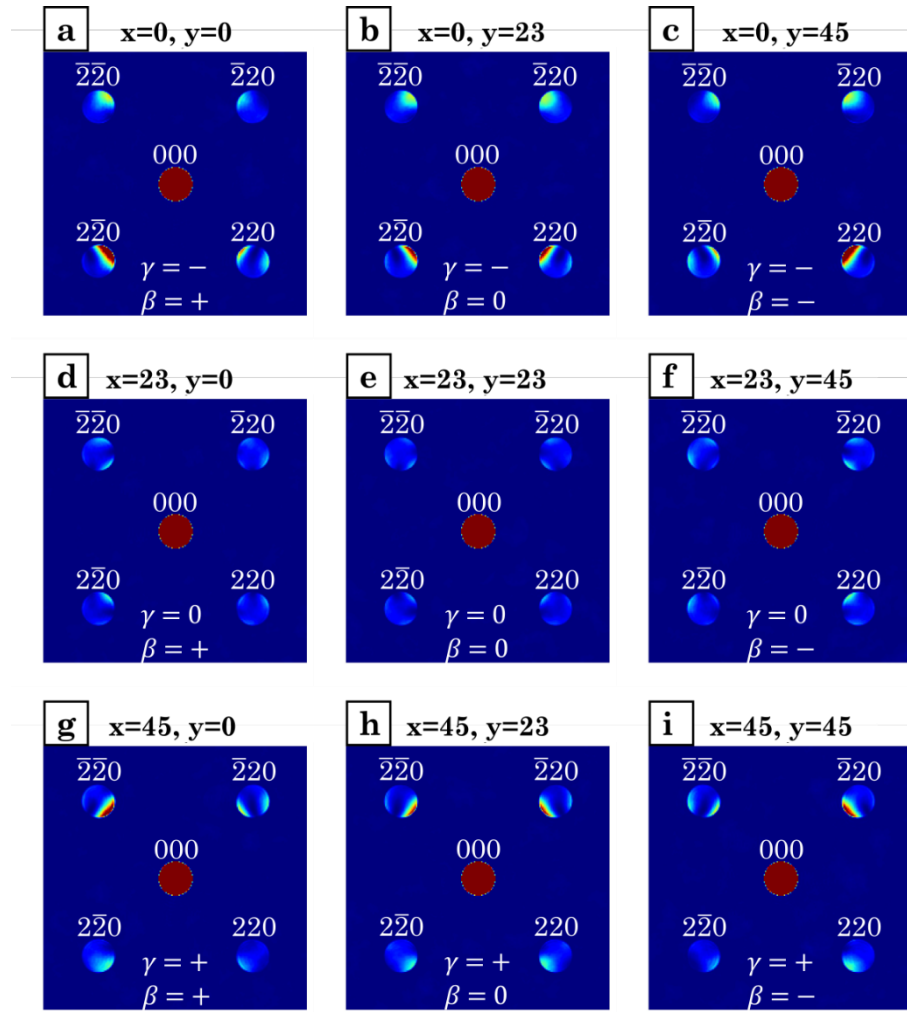
Figure 24: *Exemplary diffraction images obtained from Bending III. The position on the sample where the images were obtained are given by the indices in the headings.*

In Figure 24a the negative tilt γ is superimposed by a positive tilt β. Comparing Figures 24a and b, this superposition resulted in an even stronger excitation of the $2\bar{2}0$ disk and lighter excitations of the $\bar{2}\bar{2}0$ and 220 disks. The intensity of the $\bar{2}20$ disk, however, is lowered compared to the single tilt in Figure 24b. This resulted in no further error in the determination of ϵ_{xx} and ϵ_{yy}. However, the strain ϵ_{xy} is strongly influenced by this superposition of two tilts, yielding values as low as -0.2 %. The same behavior was found to be true for the superposition of negative γ and negative β. The intensities in Figure 24c are the ones from Figure 24a mirrored on the x-axis. Consistently, the measured strains ϵ_{xx} and ϵ_{yy} are again not further falsified compared to a simple tilt in negative γ. In contrast, ϵ_{xy} is measured to be a positive strain in the same magnitude as the negative strain in the case of a positive tilt β in Figure 24a.

In Figures 24d-f the angular deviation γ is zero and only β changes from a positive value in Figure 24d to zero in Figure 24e and finally to a negative value in Figure 24f. As the angular deviation is very small, no pronounced excitation effects can be observed. The $\bar{2}\bar{2}0$ and $2\bar{2}0$ disks in Figure 24d appear to have slightly higher intensities, which is in accordance with Figure 24a. Again, the intensities in Figure 24f are mirrored on the x-axis compared to Figure 24d, leading to very weak excitations of the $\bar{2}20$ and 220 disks. These excitations should be too small to significantly impact the strain determination.

Finally, the diffraction images obtained for positive tilts γ are presented in Figures 24g-i. The intensity distributions are like the ones in Figures 24a-c mirrored around the y-axis. For a single tilt to positive γ the $\bar{2}\bar{2}0$ and $\bar{2}20$ disks are excited (Figure 24h) leading to an underestimation of both ϵ_{xx} and ϵ_{yy} by 0.1 to 0.2 %, but again no falsification of ϵ_{xy} as in the case of negative tilts γ before. Superimposing this tilt with a positive tilt β leads to an even stronger excitation of the $\bar{2}\bar{2}0$ disk (Figure 24g), with no further error in the measurements of ϵ_{xx} and ϵ_{yy}, but ϵ_{xy} was measured about 0.15 to 0.20 % higher than the actual strain in the sample. For a superposition of positive γ and negative β, the $\bar{2}20$ disk is strongest excited (Figure 24i), resulting in the same measurement error as the combination of negative γ and positive β.

With that in mind, the measured strains are plotted over the angular deviation angle γ as illustrated in Figures 25a, c and e. The measured strains of all three specimens are in good accordance. In Figure 25a, it can be seen that the strain ϵ_{xx} starts dropping for $|\gamma|$ greater than around 1 mrad. This explains the anomaly in Section 4.2.1, where the strain in Bending II did not decrease at the boundaries in x-direction. Also, the strains ϵ_{yy} correlate remarkably good (Figure 25c), however the measured values of Bending III are set off, which might be due to the bigger outer fiber strain as already discussed in Section 4.2.2. Figure 25e proves that ϵ_{xy} does not depend on the angular deviation angle γ as long as β is zero.

Further, the influence of the tilt angle β will be discussed. Figure 25b shows the strain courses of ϵ_{xx} for all three samples. It can be seen that the strain is more or less constant over the whole range. Considering that the maximum angular deviation in Figure 25b is only 0.46 mrad, these results are in god accordance to the strain profiles over γ (Figure 25a). The same holds true for ϵ_{xy} in Figure 25f, where the strain courses are perfectly flat since γ is zero.
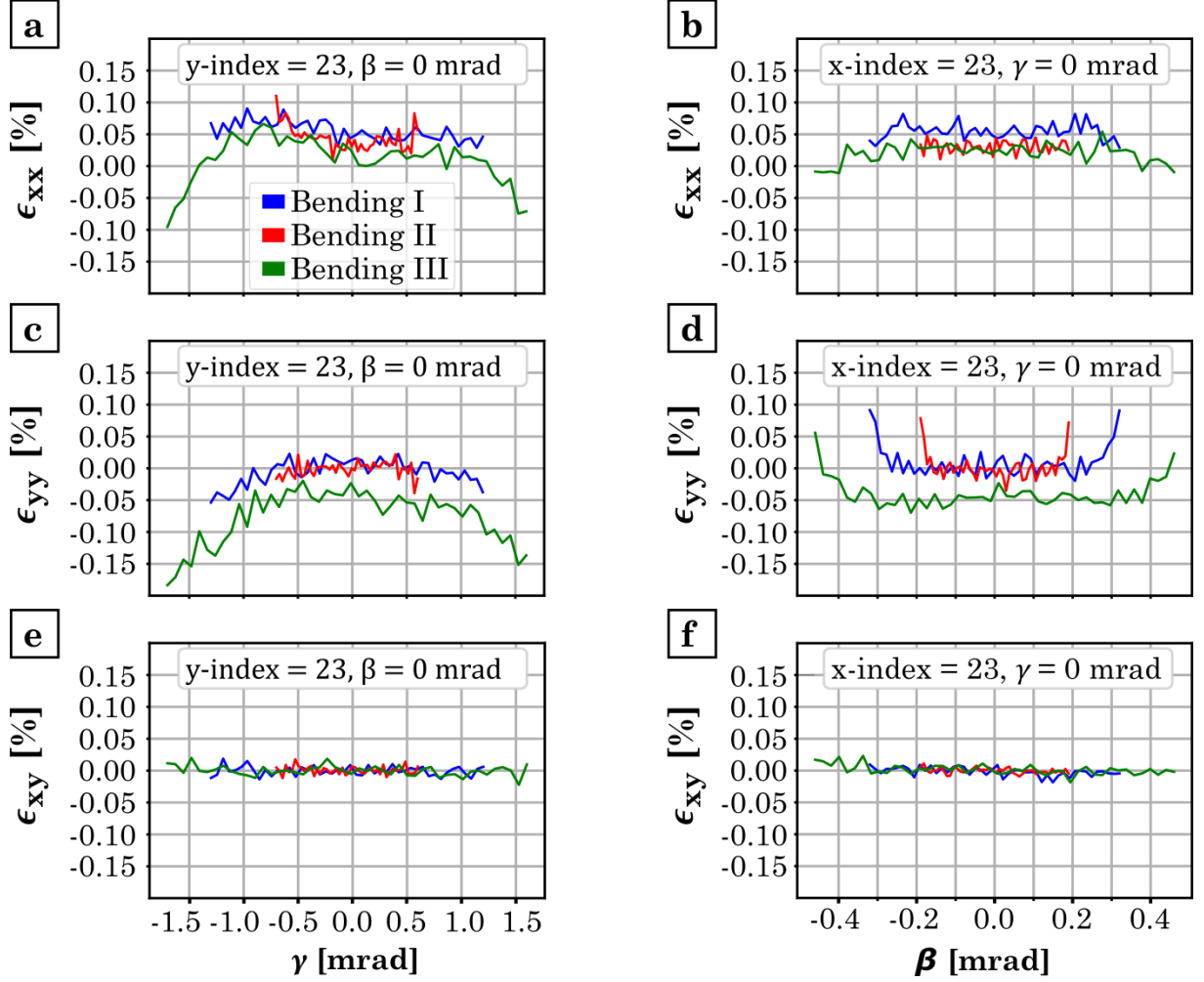
Figure 25: *Plots of the strain profiles over the angular deviation angles. a) ϵ_{xx} over γ and b) over β, c) ϵ_{yy} over γ and d) over β, e) ϵ_{xy} over γ and f) over β. The other angular deviation in each profile is zero. The legend in a) is valid for all six figures.*

However, the graphs of ϵ_{yy} in Figure 25d exhibit some inconsistencies. All three graphs show a very similar behavior along the y-axis (Figure 18b, d and f), but plotting them over β shows that the increases in strain level do not originate in the angular deviation. This effect can be traced back to the specimen itself and the image simulation. The diffraction simulations assume periodic boundary condition, which can lead to wrap around errors (compare Section 2.3.2). Due to the strain state of the sample, the dimensions in x-direction are larger than in y-direction. The supercell dimensions used for the diffraction simulation were, however, set to be squared in order to generate undistorted diffraction images with the same number of pixels in x-and y-direction. This resulted in an atom free rim as illustrated in Figure 26. The blue area indicates the size of squared supercell and the reddish dots represent the atoms, respectively their projected potential (same number of atoms in both directions!). This potential free region most likely

influenced the diffraction simulation and therefore the strain measurements at the edges of the scan region.
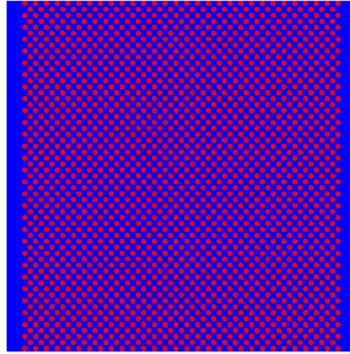
Figure 26: *Schematic illustration of one projected potential slice of the used supercells. The reddish points represent the atoms where the potential is high, and the blue areas are more or less potential free. A potential free rim on both sides can be seen, which can influence the measurements.*

4.3 Tensile specimen

In this section the results of the strain measurements of the tensile specimen are presented.

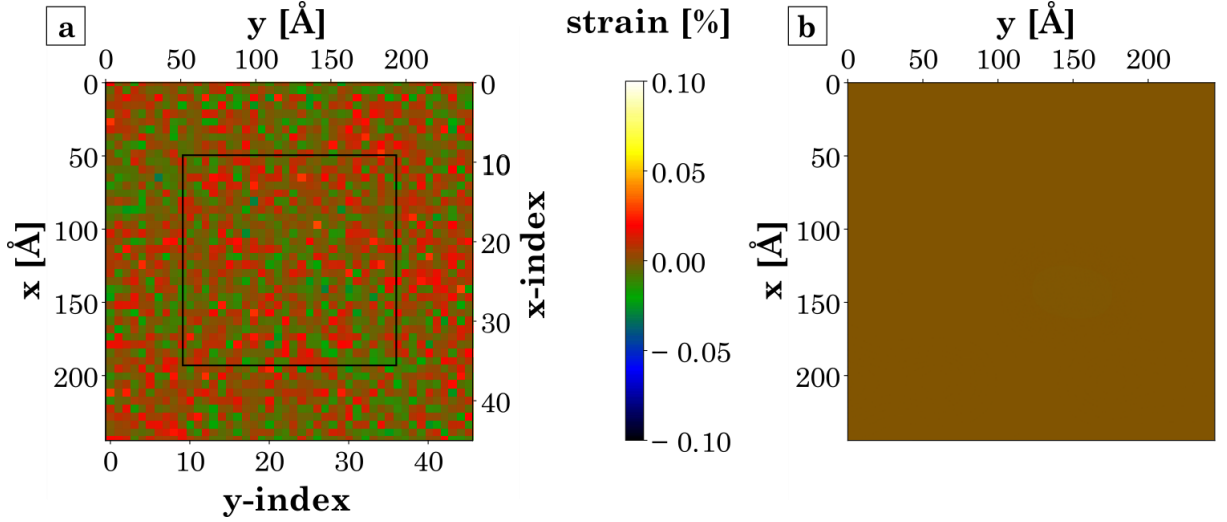### 4.3.1 Tensile specimen - ϵ_{xx}
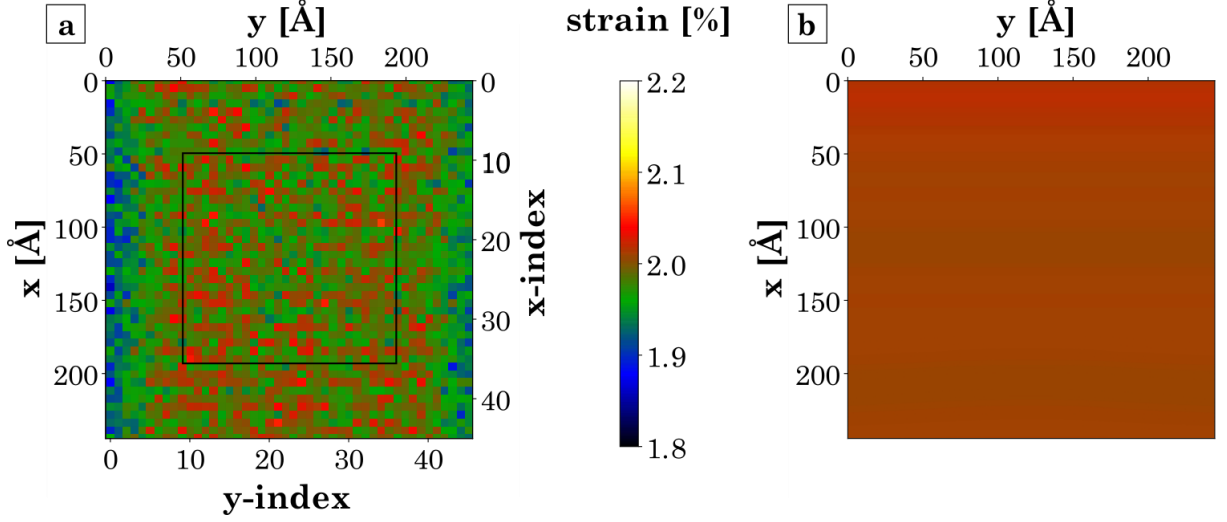
Figure 27: *Comparison between a) the ϵ_{xx} strain map obtained from the NBED simulations and b) the average strain ϵ_{xx} along the electron beam direction from the FEA.*

Figure 27 shows the comparison between the measured strain ϵ_{xx} and the arithmetic mean strain along the electron beam axis obtained from the FEA. The measured strain extends from 1.95 to 2.05 % in the middle region and falls to values around 1.90 % and lower at the boundaries in y-direction. Along the x-axis the strain level is constant with deviations in the order of the measurement precision. The strain in the map obtained from the FEA (Figure 27b) on the other hand is 2.011 % with a standard deviation of only 0.002 %.
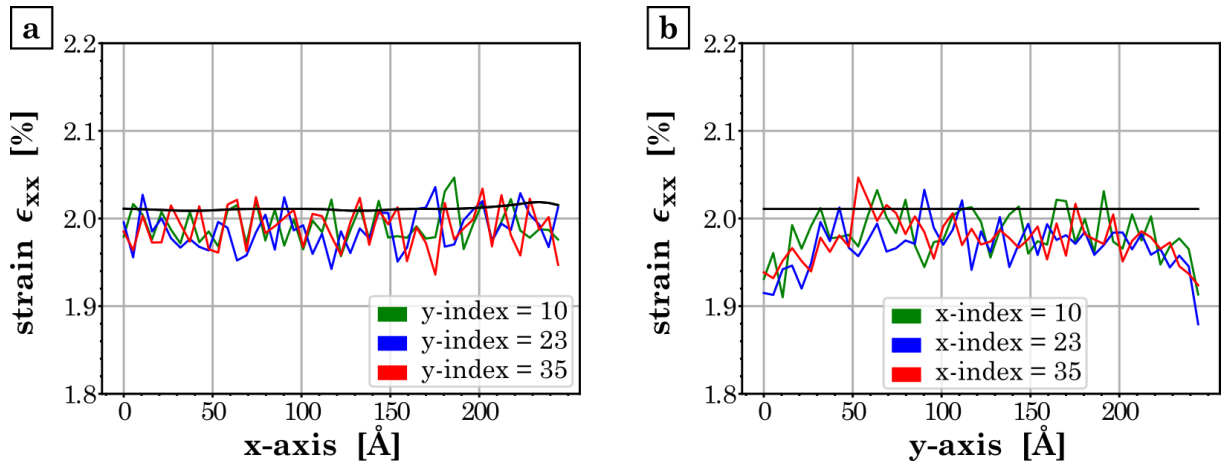
Figure 28: *ϵ_{xx} strain graphs of the tensile specimen along a) the x-axis and b) the y-axis.*

The three strain profiles along the x-axis in Figure 28a show no notable abnormalities. The measured strains are more or less constant over the whole scan region, showing deviations only in the range of typical measurement errors of around 0.05 %. In contrary to the bending samples in the section before, no drops in the measured strain are present, which can simply be explained by the fact that the [001] zone axis and the microscope optical axis align almost perfectly over the whole sample. The strain curve along the y-axis is, however, more interesting. Even though the zone axis and the microscope optical axis are aligned, the measured strain values drop below 1.90 %. This can again be traced back to the effect of the specimen dimensions and the squared supercell (compare Section 4.2.4). The broader rim here did not result in a larger error.

The histogram analysis (Figure 29) revealed that the average measured strain ϵ_{xx} is 1.988 ± 0.023 %. Hence, the measured strain is 0.023 % lower than the FEA suggests. However, this deviation is of same magnitude as the precision, so it can be stated that the measured strain is in great agreement with the arithmetic mean strain from the FEA. The fact that the standard deviation is below experimentally obtained values indicates that the simulations were accurate.
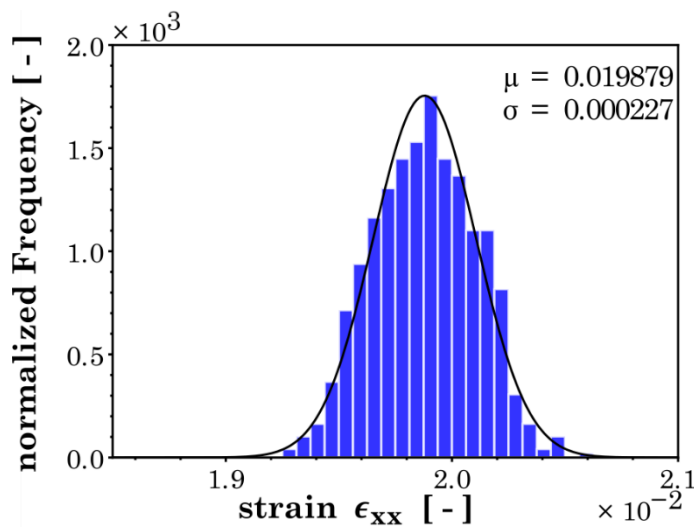
Figure 29: *Histogram analysis of the strain ϵ_{xx} of the tensile specimen.*

4.3.2 Tensile specimen - ϵ_{yy}
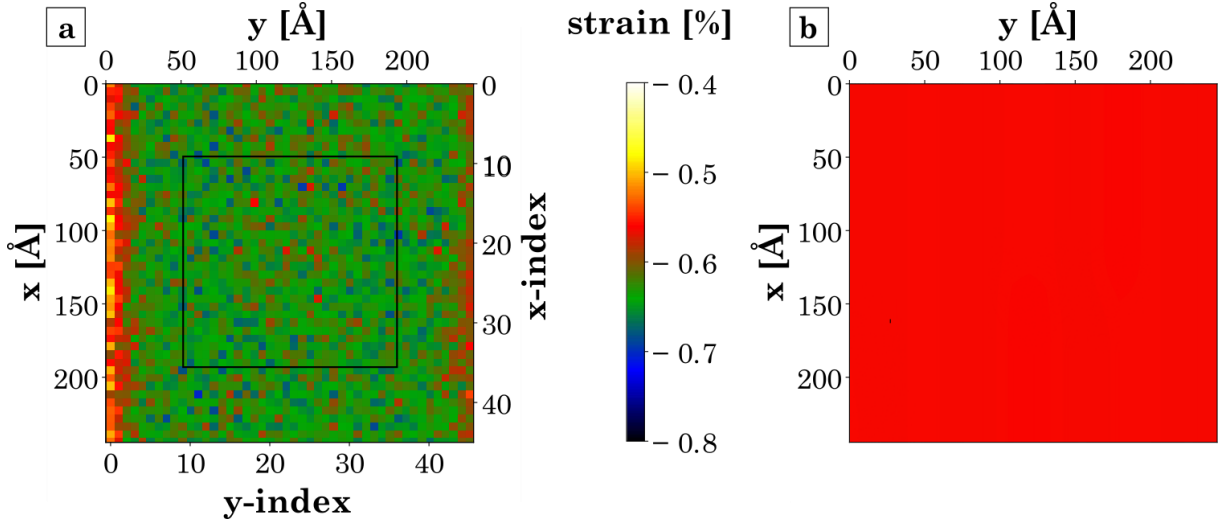
Figure 30: *Comparison between a) the ϵ_{yy} strain map obtained from the NBED simulations and b) the average strain ϵ_{yy} along the electron beam direction from the FEA.*

Figure 30 shows that the measured strain ϵ_{yy} underestimates the real strain in the sample. The measurement shows mostly values below -0.6 % (green areas) whereas the strain obtained from the FEA is -0.563 ± 0.000 %. The measurement at the boundaries in y-direction appears to be flawed again as was the case for ϵ_{xx} in Section 4.3.1. This initial impression is further visualized in Figure 31 below.
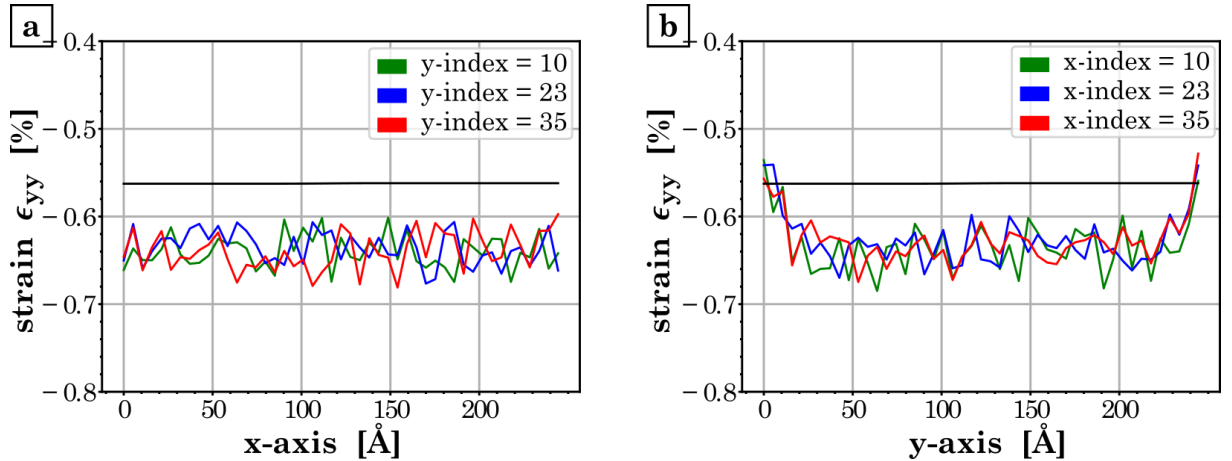
Figure 31: *ϵ_{yy} strain graphs of the tensile specimen along a) the x-axis and b) the y-axis.*

The three strain graphs along the x-axis (Figure 31a) show an almost perfectly flat course with the same deviations due to the measurement precision as in Section 4.3.1. The average strain level is around -0.65 % over the whole length with no particular conspicuities. As already visible in the strain map, the three graphs along the y-axis, presented in Figure 31b, show a flat region between 40 to 220 Å.

[41]

Outside of these regions the strain spikes towards the edges from -0.65 % up to -0.54 %. This phenomenon most likely originates again in the potential free rim in the supercell.

The histogram analysis, shown in Figure 32, revealed that the average measured strain ϵ_{yy} is -0.636 % with a precision of 0.020 %. Again, the precision suggests that the simulations are accurate, however the measurement underestimates the real strain in the sample by 0.073 %. This error in accuracy is quite large recalling that the strain ϵ_{xx} was measured with an accuracy of 0.023 %. The same result was obtained from the perfectly strained sample in Section 4.1, which leads to the assumption that there might be a systematic error in either the diffraction simulations or the strain evaluation. Unfortunately, this could not be clarified within this work.
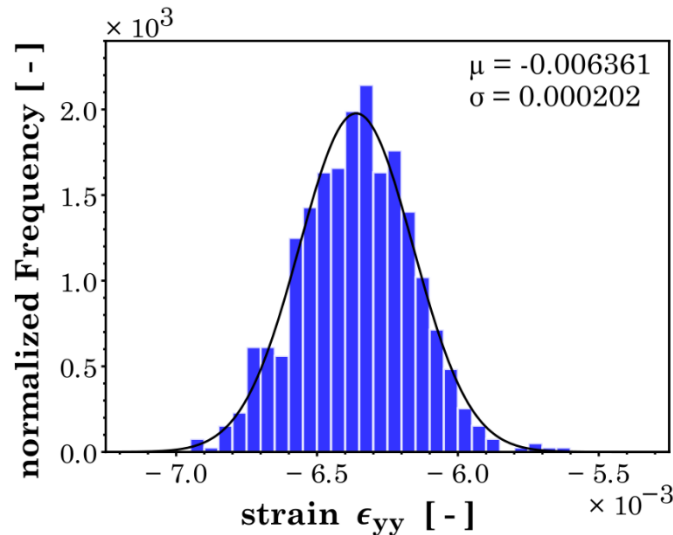
Figure 32: *Histogram analysis of ϵ_{yy} of the tensile specimen.*

[42]

4.3.3 Tensile specimen ϵ_{xy}

The results of the measurement of ϵ_{xy} are in very good agreement with the expected values. Figure 33a shows that the measurements are in the range between -0.05 and +0.05 %, with most of the results even closer to zero. The expected values from the FEA (Figure 22b) are zero over the whole scan region with deviations in the range of only 10^{-5} %. In contrast to the maps of ϵ_{xx} and ϵ_{yy} no effect due to the potential free rim can be detected.
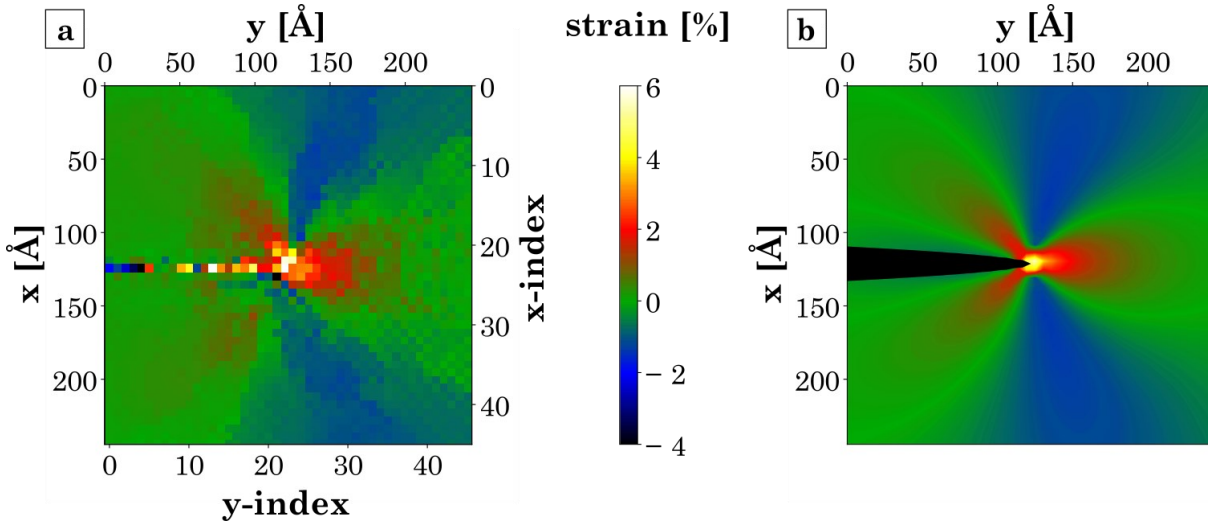

Figure 33: *Comparison between a) the ϵ_{xy} strain map obtained from the NBED simulations and b) the average strain ϵ_{xy} along the electron beam direction from the FEA for the tensile sample.*

The graphs along both the x- and y-axis in Figure 34 confirm this first impression. The measurements oscillate around zero with deviations about ± 0.02 to 0.03 %, showing no conspicuous features. Again, as described before, also the effect of the potential free rim is not visible.
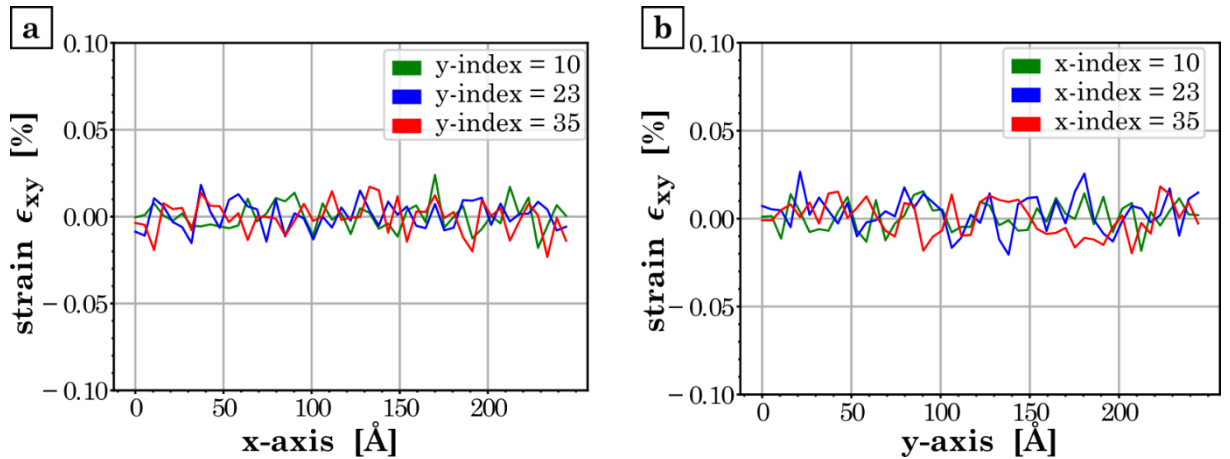
Figure 34: *ϵ_{xy} strain graphs of the tensile specimen along a) the x-axis and b) the y-axis.*

[43]

The histogram analysis presented in Figure 35 resulted in a mean strain value of 0.000 % with a precision of 0.010 %. The result is in very good accordance with the expected value and the precision of 0.010 % is extremely low compared to values found in literature.
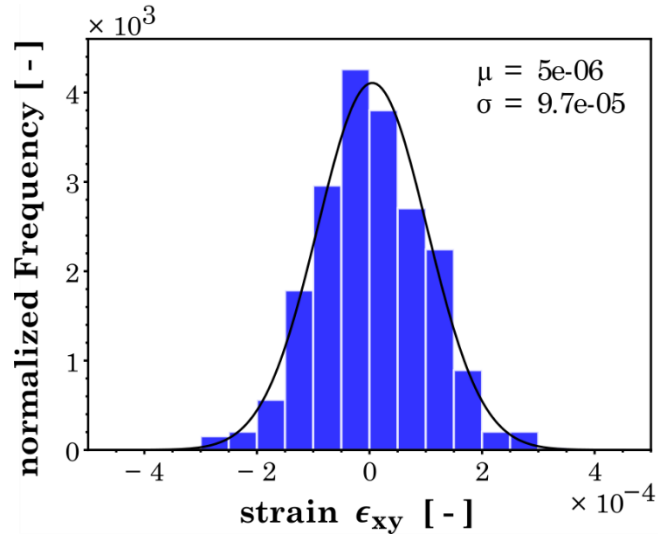
Figure 35: *Histogram analysis of ϵ_{xy} from the tensile sample.*

4.3.4 Diffraction images

For the validity of the measured results the diffraction images are analyzed. Figures 36 shows nine diffraction images obtained from the simulations. The {400} disks were cut off as they were not used in the evaluation. The positions on the sample where the images were obtained is given by the indices in the headings together with Figure 27, 30 or 33. The visual inspection of the diffraction images showed no abnormalities. The disks possess their normal intensity distributions due to dynamical diffraction, but all disks have nearly the same intensities.
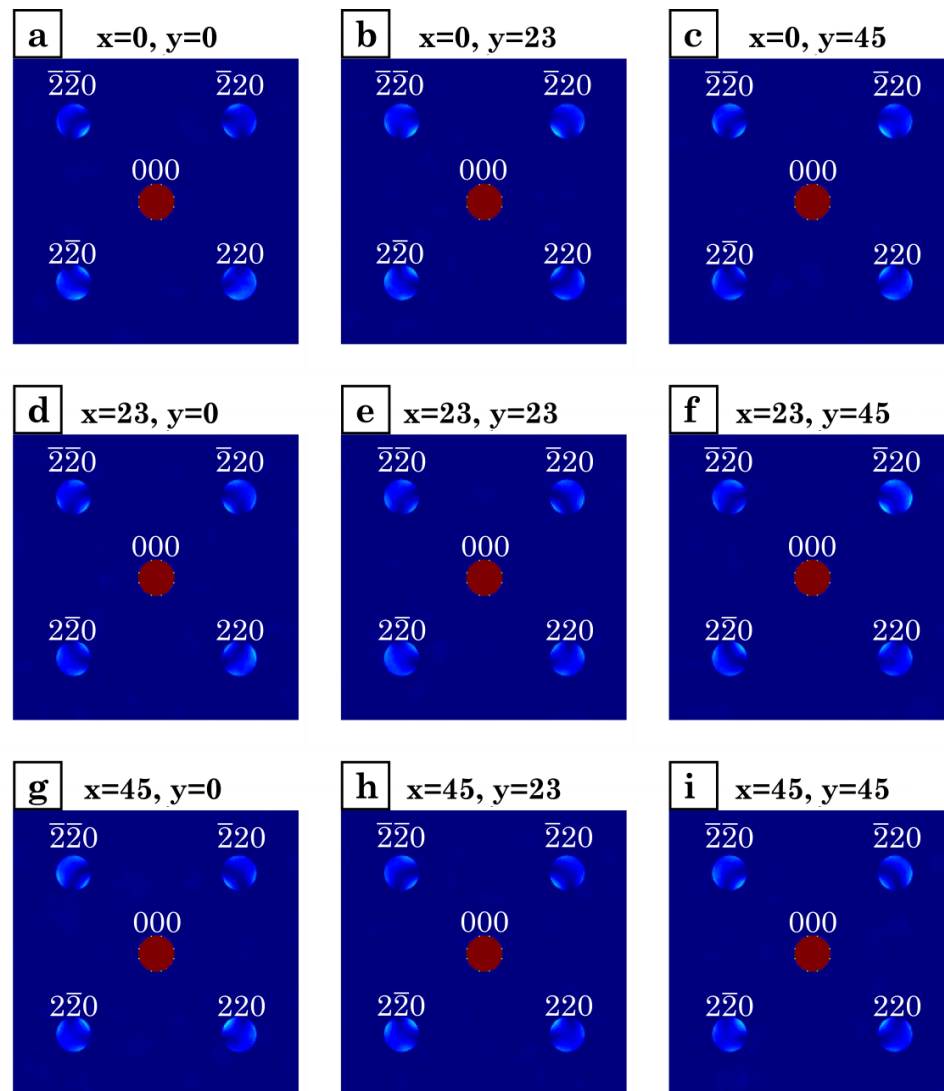
Figure 36: *Exemplary diffraction images obtained from the tensile specimen. The positions on the sample where the images were obtained are given by the indices in the headings.*

4.4 Cracked tensile specimen

In this section the results obtained from the cracked tensile sample are presented and discussed.

4.4.1 Cracked tensile sample - ϵ_{xx}

Overall, the strain field obtained by the measurement in Figure 37a is in surprisingly good accordance with the arithmetic mean strain along the electron beam direction obtained from the finite element calculations (Figure 37b). The high strain field close to the crack tip, indicated by the bright yellow portion in Figure 37b, can be identified in the measurement as well, but with a distorted shape. With increasing distance from the crack tip, the measured strain field is in better accordance with the reference.
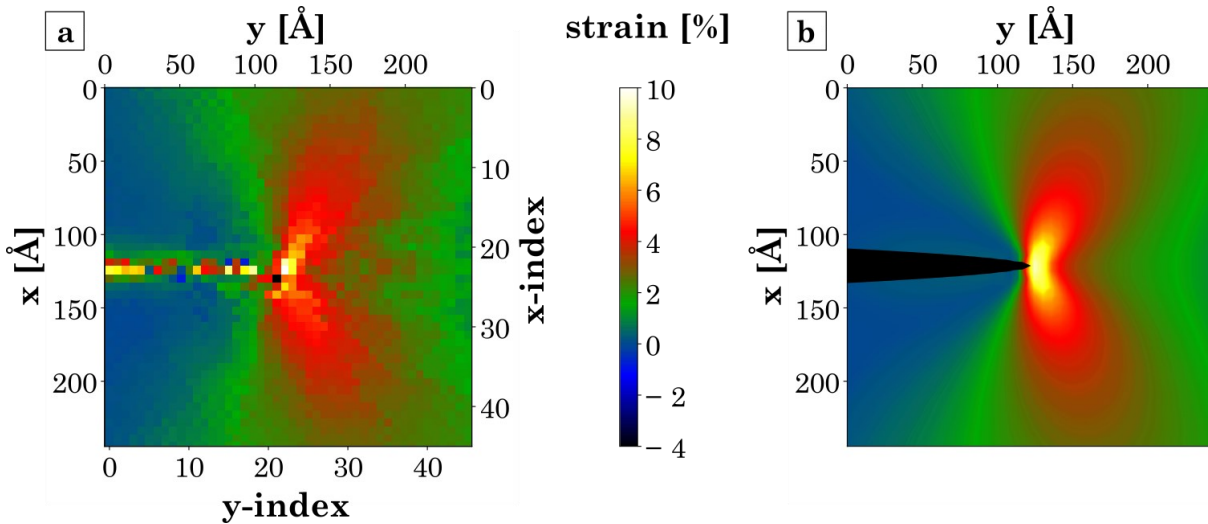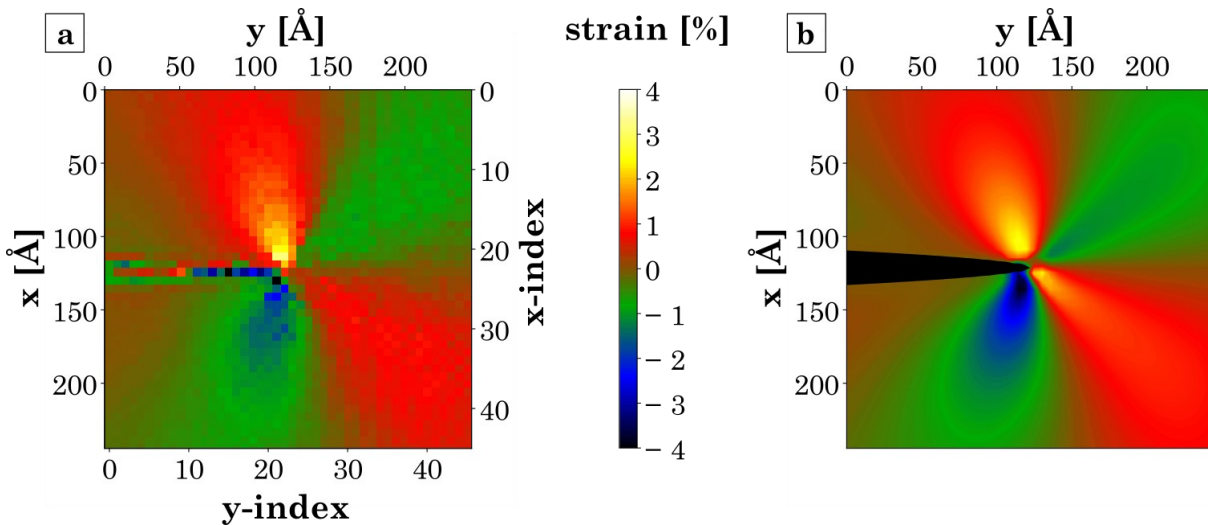

Figure 37: *Comparison between a) the ϵ_{xx} strain map obtained from the NBED simulations and b) the average strain ϵ_{xx} along the electron beam direction from the FEA. The black part in b) represents the notch.*

Figure 38 shows three strain profiles along the y axis. The measured strain is compared to the arithmetic mean strain, the strain in the top layer and the strain in the middle layer of the finite element simulations. Figures 38a and c show that the measured strain is in fact comparable to all three different strains obtained from the FEA. The measured strain shows no smooth, continuous course, which makes comparison between the measured strain and the strains obtained from the finite element analysis quite hard, especially since the different strains from the FEA differ less than the fluctuations of the measured strain. From those two figures no statement on the how the electron diffraction averages the strain can be made, but the measurement is still a good representation of the real strain state within margins.

Figure 38b shows the strain course through the crack. The measurements for x-values lower than 120 Å are not of interest as those are inside the crack. The sharp strain peak at the crack tip is strongly overestimated by around 2 % compared to the arithmetic mean strain and by about 3 % compared to the strain in the top layer of the finite element models. Right to the crack tip the measured strain drops off steeply. However, the measurements in the area close to the crack tip should be treated with caution as will be explained in Section 4.4.3.
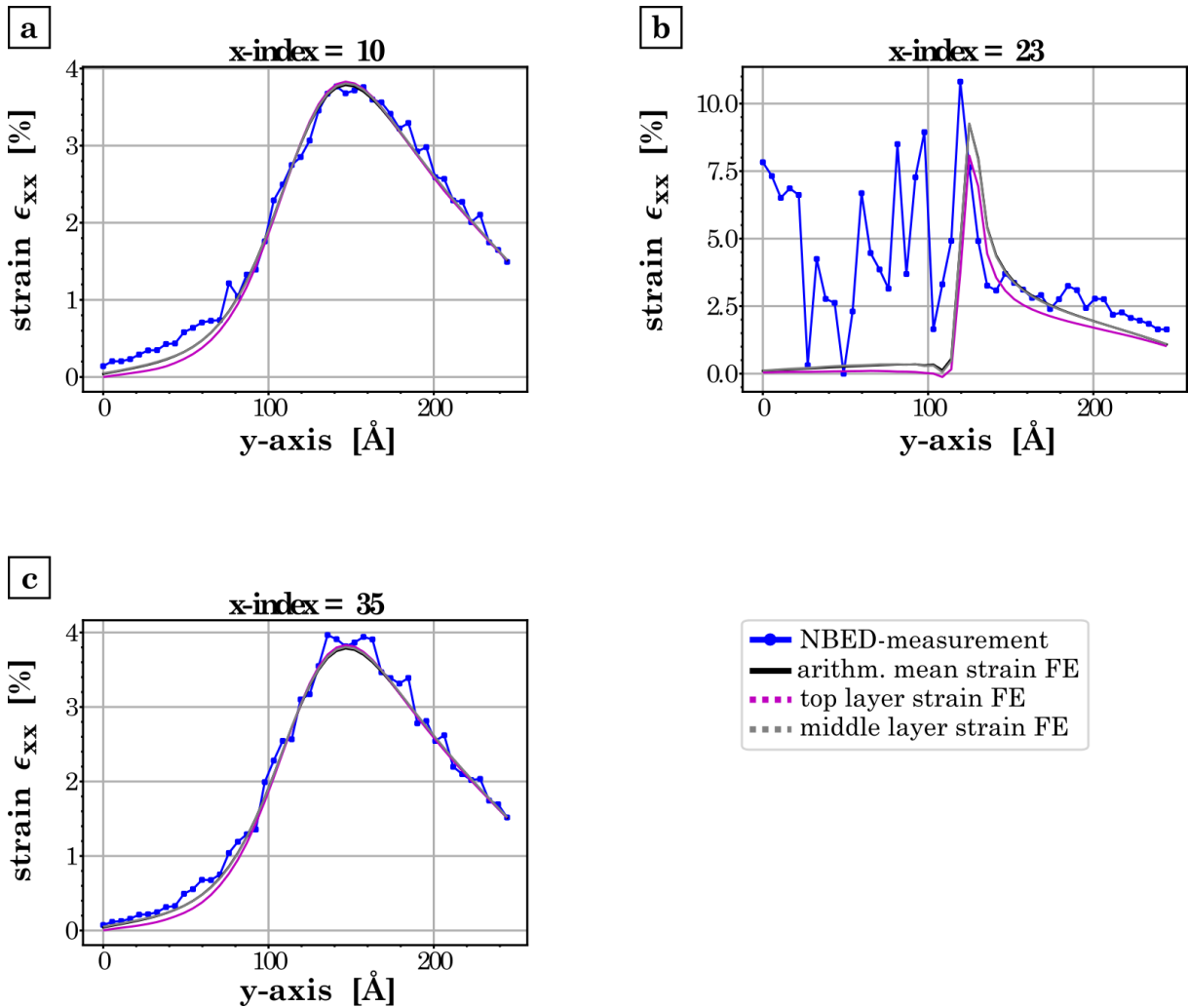
Figure 38: *Measured strain profiles ϵ_{xx} along the y-axis for three different x-indices.*

4.4.2 Cracked tensile specimen – ϵ_{yy}

The ϵ_{yy} strain field of the measurement in Figure 39a shows the same trend as the arithmetic mean strain from the FEA illustrated in Figure 39b. The areas with negative strain values (blue regions) are clearly reproduced in the same manner and also the tensile region right to the crack tip is clearly evident, even though it appears broadened compared to the reference. The areas experiencing tension in negative and positive x-direction next to the crack appear broadened and disturbed as well.

Figure 39: *Comparison between a) the ϵ_{yy} strain map obtained from the NBED simulations and b) the average strain ϵ_{yy} along the electron beam direction from the FEA.*

Strain profiles along the y-axis were created and for comparison the arithmetic mean strain, the strain in the top layer and the strain in the middle layer are shown. The profiles for x-indices 10 and 35 are quite similar (Figures 40a and c). Overall, the measured strain can best be approximated with the arithmetic mean strain in the sample, however, the measured strain is slightly higher compared to the three different strains from the FEA. Especially, in the regions with a strong strain gradient in y-direction (between 80 to 140 Å), the measurement seems to overestimate the real strain by up to 0.5 %. For small y-values the measured strain is best comparable to the strain in the middle layer of the specimen. There, the arithmetic mean strain and the strain in the middle layer however differ less than 0.1 %, thus both are capable of describing the measured strain profile. Figure 40b shows the strain profile through the crack, hence the measurements left to the sharp peak are neglected. The height of the peak is strongly overestimated by around 7 % compared to the arithmetic mean strain. This originates most likely in the free surface due to the crack in this area, strongly influencing the diffraction

simulation. For higher x-values, the measured strain is again in very good agreement with the arithmetic mean strain from the FEA. The maximum deviation is of magnitude 0.5 %.
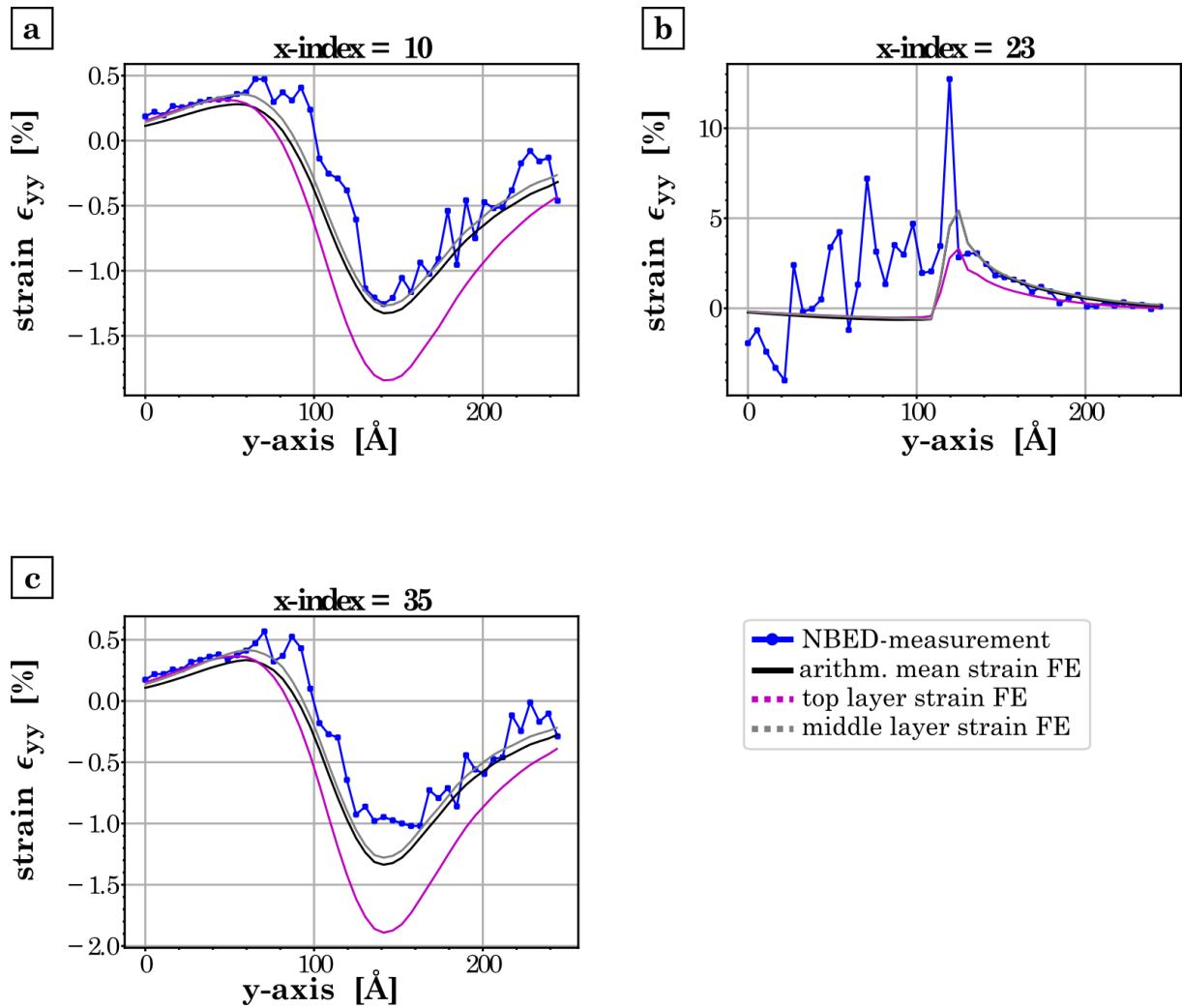
Figure 40: *Measured strain profiles ϵ_{yy} along the y-axis for three different x-indices.*

4.4.3 Cracked tensile specimen - ϵ_{xy}

The results of the diffraction simulation in Figure 41a replicated the strain field obtained from the FEA (Figure 41b) quite good, as all characteristics are present. However, the magnitudes of the measured strains are slightly lower. The blue area below the notch is visible, but the dark blue part from the FEA is not present in the measurement. The same holds true for the red area below the notch and the green area above. Interestingly, in the red area above the crack the strain magnitude of the measurement is in extremely good accordance with the reference. In the notch area, the measurement breaks down again, as expected.

Figure 41: *Comparison between a) the ϵ_{xy} strain map obtained from the NBED simulations and b) the average strain ϵ_{xy} along the electron beam direction from the FEA.*

The strain profiles in Figures 42a and c show that the course of the measured strain reproduces the strains of the FEA rather good. Especially for small y-values, where the strain in the specimen is close to zero, the measurement supplies an equivalent result. Interestingly, also the strong gradient between 120 to 160 Å is extremely well reproduced. However, in these areas, the strain gradient along the optical axis is negligible as all three FE-strains fall together. In the areas with higher absolute strain values (around 50 to 100 Å and 160 to 240 Å) the FE-strains are further apart due to a higher strain gradient along the electron beam direction. There the absolute value of the measured strain is about 0.2 to 0.4 % smaller compared to the arithmetic mean strain.

The strain profile through the crack tip is shown in Figure 42b. The sharp peak at around 120 Å indicates the crack tip, leaving all measurements to the left out of interest. Exactly at the crack tip, the strain ϵ_{xy} is measured about 1.5 % to low, which can be traced back to the influence of the crack itself, as can be seen in the

next section. For larger x-values the measurement is in better agreement with the reference, but still deviates by around -0.2%.
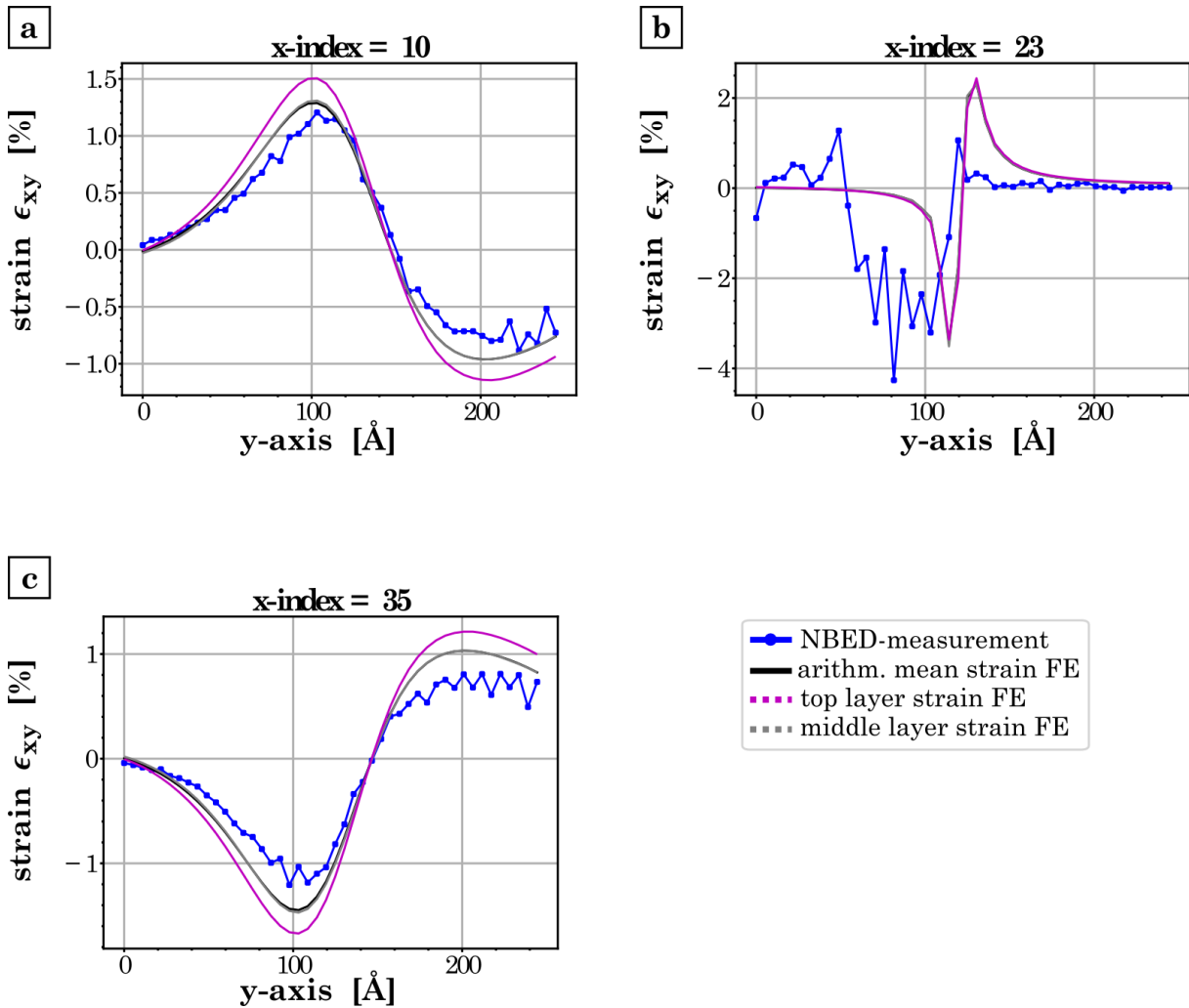
Figure 42: *Measured strain profiles ϵ_{xy} along the y-axis for three different x-indices.*

4.4.4 Diffraction images

In Figure 43 exemplary diffraction images obtained from the cracked tensile specimen are presented. It is visible that the large strains and strain gradients pushed the diffraction simulation to its limits. In Figures 43a and g the strains are comparably low, thus the simulation still delivered sufficient results. In both cases the $\bar{2}\bar{2}0$ and $2\bar{2}0$ disks were strongly excited. With the results from Section 4.2 it can be expected that the strains ϵ_{xx} and ϵ_{yy} are measured falsely by at least 0.2 % or probably even more as the excitation is fairly strong. In Figures 43b and h the diffraction simulation is already expected to deliver falsified results, as forbidden diffraction disks appear visible. These disks cannot be assigned to specific planes but rather appear randomly. Furthermore, the $\bar{2}\bar{2}0$ and $2\bar{2}0$ disks are excited, leading to an additional source of error in the evaluation. The forbidden disks are also present in Figures 43c and i. Figure 43d was obtained inside the crack, where no atoms were present. Nevertheless, the {220} disks were slightly visible. Furthermore, the central beam disk 000 is broadened. At the crack tip the diffraction simulation provides strongly disturbed images (Figure 43e). The {220} peaks are washed-out, entirely losing their disk shape. In addition, a strong background noise is present. Further right from the crack tip, the diffraction image still contains a lot of background noise with a characteristic pattern (Figure 42f). Nonetheless, even for these extreme conditions the strain measurement provided a good description of the real strain in the sample.
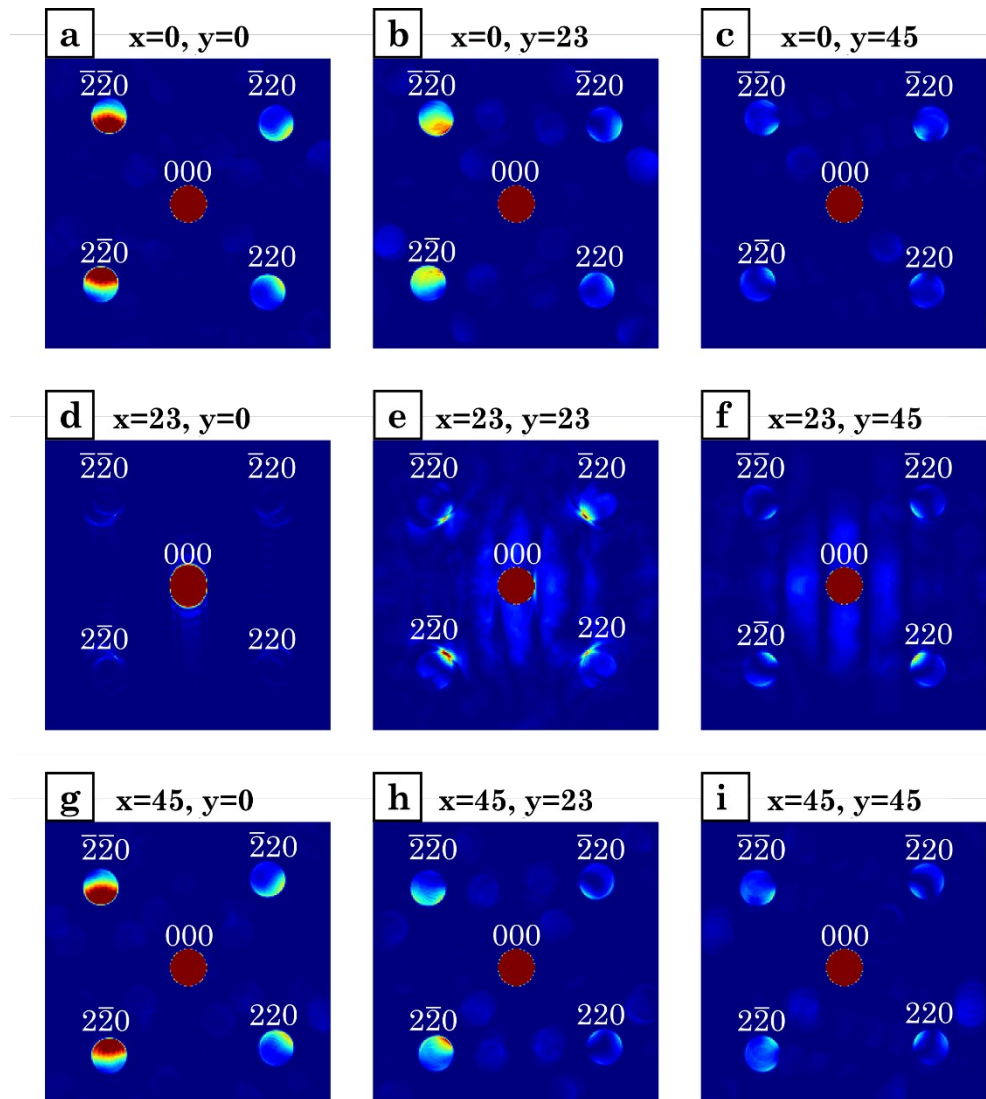
Figure 43: *Exemplary diffraction images obtained from the cracked tensile specimen. The positions on the sample where the images were obtained are given by the indices in the headings.*

5 Conclusion

In this study the effect of three-dimensional strain fields on the strain measurement using NBED was examined. Since there are to date no studies on this topic, this thesis aims to increase the understanding of the averaging process by dynamical diffraction.

First of all, it could be shown that STEM image simulations can be used to determine strains in samples with far higher precisions and accuracies compared to experimentally achievable ones and might provide a powerful tool to verify experimentally obtained results.

The results of the cantilever bending beam indicate that the measured strain is in very good accordance with the arithmetic mean strain along the electron beam direction. However, the absolute values differ by about 0.01 to 0.05 % from this reference strain. In the simulations here, no correlation between the magnitude of the outer fiber strains and the absolute values of the measured strain could be found. Dependent on whether the imaging electrons enter the specimen in the tensile or compression region determines the sign of the measured strain. If the electrons enter the tensile region of the specimen, the measured strain is slightly tensile as well, whereas a compressive strain is measured if the electrons enter the compression region first.

Further the influence of specimen tilt due to the bend was investigated. Tilting the specimen led to a strong excitation of specific diffraction disks which further falsified the strain measurement. Up to tilt angles of around 1 mrad the measured strain was more or less constant but started dropping for greater tilts. Tilts up to 1.7 mrad around the y-axis where measured and led to underestimations of the strains ϵ_{xx} and ϵ_{yy} of up to 0.2 %. All three samples showed the same dependency on the tilt angle, where the decrease in the strain levels is not linearly dependent on the tilt angle. In addition, tilts around the x-axis of up to 0.46 mrad were present in the samples, which had no influence on the measured strain. The measurement of shear strains ϵ_{xy} is not influenced by a single tilt direction, as it excites two neighboring diffraction disks equally. A superposition of two tilts around different axes, however, resulted in a stronger excitation of one single diffraction disk, which resulted in a falsification of the measurement. Depending on the tilting direction, ϵ_{xy} is either over- or underestimated.

The results of the tensile specimen were in very good accordance with the arithmetic mean strain along the microscope optical axis of the finite element

simulations, deviating only by 0.023 % for ϵ_{xx}, 0.073 % for ϵ_{yy} and 0.000 % for ϵ_{xy}. The results are all within margin of typical measurement accuracies.

In the case of the cracked tensile sample, the strain gradients were extremely high, especially along the x- and y-direction. In the resulting diffraction images strong distortions were present, ranging from very strong excitations in regions with lower strain gradients to completely washed-out disks in the areas closer to the crack tip. In these areas the measured strains ϵ_{xx} and ϵ_{yy} were about 0.5 % off the arithmetic mean strain and roughly up to 1 % off the maximum strain in the specimen. Unfortunately, this specimen did not allow for a clear statement on how the strain is averaged in NBED experiments. Nevertheless, evaluating the images using the square-root magnitude weighted phase correlation method still resulted in a good agreement between the reference strains and the strain maps, demonstrating the stability of this technique.

To conclude, the measured strains are well described by the arithmetic mean strain along the microscope optical axis. There are small deviations for the cantilever bending beam with the sign depending on the strain in the initial penetration region. For the tensile specimen, good results were obtained during the entire simulation process. Although the diffraction simulation for the cracked tensile specimen was brought to its limits, the measured strain was still in good accordance with the arithmetic mean strain.

List of figures

List of tables

References

[1] D. Yu, Y. Zhang, F. Liu, First-principles study of electronic properties of biaxially strained silicon: Effects on charge carrier mobility, Phys. Rev. B 78 (2008) 245204.

[2] A. Béché, J.L. Rouvière, J.P. Barnes, D. Cooper, Strain measurement at the nanoscale: Comparison between convergent beam electron diffraction, nanobeam electron diffraction, high resolution imaging and dark field electron holography, Ultramicroscopy 131 (2013) 10–23.

[3] M.J. Hÿtch, A.M. Minor, Observing and measuring strain in nanostructures and devices with transmission electron microscopy, MRS Bull. 39 (2014) 138–146.

[4] S.E. Zeltmann, A. Müller, K.C. Bustillo, B. Savitzky, L. Hughes, A.M. Minor, C. Ophus, Patterned probes for high precision 4D-STEM bragg measurements, Ultramicroscopy 209 (2020) 112890.

[5] J.-L. Rouviere, A. Béché, Y. Martin, T. Denneulin, D. Cooper, Improved strain precision with high spatial resolution using nanobeam precession electron diffraction, Appl. Phys. Lett. 103 (2013) 241913.

[6] C.B. Carter, D.B. Williams, "Transmission Electron Microscopy", Springer International Publishing, Cham, 2016, 149.

[7] S. Takagi, A Dynamical Theory of Diffraction for a Distorted Crystal, Journal of the Physical Society of Japan 26 (1969) 1239–1253.

[8] I. Lobato, D. van Dyck, MULTEM: A new multislice program to perform accurate and fast electron diffraction and imaging simulations using Graphics Processing Units with CUDA, Ultramicroscopy 156 (2015) 9–17.

[9] E.J. Kirkland, "Advanced Computing in Electron Microscopy", Springer US, Boston, 2010, 77-96, 115-145

[10] C.J. Humphreys, The scattering of fast electrons by crystals, Reports o Progress in Physics 42, (1979), 1825-1887

[11] B.G. Mendis, "Electron Beam-Specimen Interactions and Simulation Methods in Microscopy", John Wiley & Sons Ltd, 2018, 93-97.

[12] H. Bethe, Theorie der Beugung von Elektronen an Kristallen, Ann. Phys. 392 (1928) 55-129.

[13] F. Bloch, Über die Quantenmechanik der Elektronen in Kristallgittern, Zeitschrift für Physik 52 (1929) 555-600.

[14] C. Birkeland, R. Holmestada, K. Marthinsenb, R. Hoiera, Efficient beam-s election criteria in quantitative convergent beam electron diffraction, Ultramicroscopy 66 (1996) 89–99.

[15] Y. Ma, L.D. Marks, Bloch-wave solution in the Bragg case, Acta Cryst A45 (1989) 174–182.

[16] A. Howie, M. J. Whelan, Diffraction contrast of electron microscope images of crystal lattice defects - II. The development of a dynamical theory, Proc. R. Soc. Lond. A 263 (1961) 217–237.

[17] A General Matrix Representation of the Dynamical Theory of Electron Diffraction I. General Theory, Proc. R. Soc. Lond. A 431 (1990), 111-123.

[18] L. Sturkey, The Calculation of Electron Diffraction Intensities, Proc. R. Soc. Lond. A 80 (1962) 321-354

[19] J.M. Cowley, A.F. Moodie, The scattering of electrons by atoms and crystals. I. A new theoretical approach, Acta. Cryst. 10 (1957) 609-619.

[20] JEOL, glossary, Keywords "weak phase object approximation" | Keywords | Glossary of TEM Terms | JEOL, January 2021.

[21] L. Reimer, H. Kohl, "Transmission electron microscopy: Physics of image formation", Springer, New York, 2008,

[22] G. Kirchhoff, Zur Theorie der Lichtstrahlen, Ann. Phys. 254 (1883) 663-695.

[23] C. Ophus, A fast image simulation algorithm for scanning transmission electron microscopy, Adv. Struct. Chem. Imaging 3 (2017) 13.

[24] Chegg Study , https://www.chegg.com/homework-help/list-point-coordinates -atoms-associated-diamond-cubic-unit-c-chapter-3-problem-24qp-solution- 9780470556733-exc , January 2021.

[25] M.A. Hopcroft, W.D. Nix, T.W. Kenny, What is the Young's Modulus of Silicon?, J. Microelectromech. Syst. 19 (2010) 229–238.

[26] A. Masolin, P.-O. Bouchard, R. Martini, M. Bernacki, Thermo-mechanical and fracture properties in single-crystal silicon, J Mater Sci 48 (2013) 979–988.

[27]   C. Spura, „Einführung in die Balkentheorie nach Timoshenko und Euler-Bernoulli", Springer Fachmedien Wiesbaden, Wiesbaden, 2019, 17

[28]   O.A. Bauchau, J.I. Craig, Structural analysis: With applications to aerospace structures, Springer, Dordrecht, New York, 2009, 174f

[29]   C. Ophus, "Atomic coordinate input format for Prismatic, Input File Format (prism-em.com), July 2020.

[30]   D.A. Mullera, B. Edwards, E.J. Kirkland, J. Silcox, Simulation of thermal diffuse scattering including a detailed phonon dispersion curve, Ultramicroscopy 86 (2001) 371–380.

[31]   A. Pryor JR., C. Ophus, J. Miao, A Streaming Multi-GPU Implementation of Image Simulation Algorithms for Scanning Transmission Electron Microscopy, *Adv Struct Chem Imag* **3** (2017) 15.

[32]   P.G. Self, M.A. O´Keefe, P.R. Buseck, A.E.C. Spargo, Practical computation of amplitudes and phases in electron diffraction, Ultramicroscopy 11 (1983) 35–52.

[33]   T.C. Pekin, C. Gammer, J. Ciston, A.M. Minor, C. Ophus, Optimizing disk registration algorithms for nanobeam electron diffraction strain mapping, Ultramicroscopy 176 (2017) 170–176.

[34]   V.B. Ozdol, C. Gammer, X.G. Jin, P. Ercius, C. Ophus, J. Ciston, A.M. Minor, Strain mapping at nanometer resolution using advanced nano-beam electron diffraction, Appl. Phys. Lett. 106 (2015), 253107.

[35]   C. Mahr, K. Müller-Caspary, T. Grieb, M. Schowalter, T. Mehrtens, F.F. Krause, D. Zillmann, A. Rosenauer, Theoretical study of precision and accuracy of strain analysis by nano-beam electron diffraction, Ultramicroscopy 158 (2015) 38–48.

[36]   A. Béché, J.L. Rouvière, L. Clément, J.M. Hartmann, Improved precision in strain measurement using nanobeam electron diffraction, Appl. Phys. Lett. 95 (2009) 123114.

[37]   K. Usuda, T. Numata, T. Irisawa, N. Hirashita, S. Takagi, Strain characterization in SOI and strained-Si on SGOI MOSFET channel using nano-beam electron diffraction (NBD), Materials Science and Engineering: B 124-125 (2005) 143–147.

[38] A. Hähnel, M. Reiche, O. Moutanabbir, H. Blumtritt, H. Geisler, J. Höntschel, H.-J. Engelmann, Improving accuracy and precision of strain analysis by energy-filtered nanobeam electron diffraction, Microsc. Microanal. 18 (2012) 229–240.

[39] T. Grieb, F.F. Krause, M. Schowalter, D. Zillmann, R. Sellin, K. Müller-Caspary, C. Mahr, T. Mehrtens, D. Bimberg, A. Rosenauer, Strain analysis from nano-beam electron diffraction: Influence of specimen tilt and beam convergence, Ultramicroscopy 190 (2018) 45–57.

[40] C. Mahr, K. Müller-Caspary, M. Graf, A. Lackmann, T. Grieb, M. Schowalter, F.F. Krause, T. Mehrtens, A. Wittstock, J. Weissmüller, A. Rosenauer, Measurement of local crystal lattice strain variations in dealloyed nanoporous gold, Materials Research Letters 6 (2018) 84–92.

[41] D. Cooper, T. Denneulin, N. Bernier, A. Béché, J.-L. Rouvière, Strain mapping of semiconductor specimens with nm-scale resolution in a transmission electron microscope, Micron 80 (2016) 145–165.